Monthly Notices
of the
ROYAL ASTRONOMICAL SOCIETY
MNRAS **455,** 1341–1363 (2016) doi:10.1093/mnras/stv2048

Hunting for brown dwarf binaries and testing atmospheric models with X-Shooter

E. Manjavacas,[1,2⋆] B. Goldman,[2,3] J. M. Alcalá,[4] M. R. Zapatero-Osorio,[5] V. J. S. Béjar,[1,6] D. Homeier,[7,8] M. Bonnefoy,[9,10] R. L. Smart,[11] T. Henning[2] and F. Allard[8]

[1]*Instituto de Astrofísica de Canarias, C/ Vía Láctea, s/n, E-38205 La Laguna (Tenerife), Spain*
[2]*Max Planck Institute für Astronomie, Königstuhl 17, D-69117 Heidelberg, Germany*
[3]*Observatoire astronomique de Strasbourg, Université de Strasbourg, 11 rue de l'Université, F-67000 Strasbourg, France*
[4]*INAF - Osserv. Astronomico di Capodimonte, Via Moiariello 16, I-80131 Napoli, Italy*
[5]*Centro de Astrobiología (CSIC-INTA), Carretera de Ajalvir km 4, E-28850 Torrejón de Ardoz, Madrid, Spain*
[6]*Universidad de La Laguna, Dpto. Astrofísica, E-38206 La Laguna (Tenerife), Spain*
[7]*Zentrum für Astronomie der Universität Heidelberg, Landessternwarte Königstuhl 12, D-69117 Heidelberg, Germany*
[8]*CRAL-ENS, 46, Allée d'Italie, F-69364 Lyon Cedex 07, France*
[9]*Univ. Grenoble Alpes, IPAG, F-38000 Grenoble, France*
[10]*CNRS, IPAG, F-38000 Grenoble, France*
[11]*Instituto Nazionale di Astrofisica, Osservatorio Astrofisico di Torino, Strada Osservatorio 20, I-10025 Pino Torinese, Italy*

Accepted 2015 September 1. Received 2015 September 1; in original form 2015 June 19

ABSTRACT

The determination of the brown dwarf binary fraction may contribute to the understanding of the substellar formation mechanisms. Unresolved brown dwarf binaries may be revealed through their peculiar spectra or the discrepancy between optical and near-infrared spectral-type classification. We obtained medium-resolution spectra of 22 brown dwarfs with these characteristics using the X-Shooter spectrograph at the Very Large Telescope. We aimed to identify brown dwarf binary candidates, and to test if the BT-Settl 2014 atmospheric models reproduce their observed spectra. To find binaries spanning the L–T boundary, we used spectral indices and compared the spectra of the selected candidates to single spectra and synthetic binary spectra. We used synthetic binary spectra with components of same spectral type to determine as well the sensitivity of the method to this class of binaries. We identified three candidates to be combination of L plus T brown dwarfs. We are not able to identify binaries with components of similar spectral type. In our sample, we measured minimum binary fraction of $9.1^{+9.9}_{-3.0}$ per cent. From the best fit of the BT-Settl models 2014 to the observed spectra, we derived the atmospheric parameters for the single objects. The BT-Settl models were able to reproduce the majority of the spectral energy distributions from our objects, and the variation of the equivalent width of the Rb I (794.8 nm) and Cs I (852.0 nm) lines with the spectral type. None the less, these models did not reproduce the evolution of the equivalent widths of the Na I (818.3 and 819.5 nm) and K I (1253 nm) lines with the spectral type.

Key words: stars: low-mass – brown dwarfs – binaries: spectroscopic.

1 INTRODUCTION

Stars are believed to be born in large stellar nurseries, which they eventually leave to form the field population. A large number of stars remain in binary or hierarchical systems. Multiplicity provides constraints on fundamental parameters, such as dynamical masses, essential to test atmospheric and substellar formation models. It is well known that the binary fraction decreases when decreasing mass. This fraction decreases from 80–60 per cent for O and B stars, to 40 per cent for the M dwarfs (Janson et al. 2012). The decreasing trend for binarity seems to extend to the substellar regime. For L and T brown dwarfs, the binary fraction is estimated at about 20 per cent (Bouy et al. 2003; Burgasser et al. 2003; Close et al. 2003; Gizis et al. 2003; Burgasser, Cruz & Kirkpatrick 2007; Luhman et al. 2007; Goldman et al. 2008).

⋆ E-mail: manjavacas@iac.es

Based on Monte Carlo simulations, Allen (2007) determined that 98 per cent of the brown dwarf binaries have separations smaller than 20 au. Burgasser et al. (2007) pointed out that the peak of the separation distribution of brown dwarfs is ∼3 au, which is very close to the limit of the high-resolution imaging surveys. Allen (2007) estimated that a fraction of ∼6–7 per cent of brown dwarf binary systems have not been detected yet, as a consequence of observational biases. For instance, Joergens (2008) searched for low-mass stars and brown dwarfs binaries in the Chameleon star-forming region using the radial velocity method, and concluded that the percentage of brown dwarfs binary systems with separations below 1 au is less than ∼10 per cent in this star-forming region. Blake, Charbonneau & White (2010) monitored a sample of 59 ultracool dwarfs with radial velocity and determined that the binary frequency of low-mass unresolved systems is $2.5^{+8.6}_{-1.6}$ per cent.

Spectroscopic data provide also important constraints to atmospheric models. These models allow us to disentangle the effect of varying effective temperature, gravity, and metallicity on the spectral features. Below an effective temperature of ∼2600 K, models predict that clouds of iron and silicate grains begin to form, affecting the opacity (Lunine, Hubbard & Marley 1986; Tsuji et al. 1996; Burrows & Sharp 1999; Lodders 1999; Marley 2000; Allard et al. 2001; Marley et al. 2002). Self-consistent atmospheric models, such as the BT-Settl models (Allard, Homeier & Freytag 2012b) and the Drift-PHOENIX models (Helling et al. 2008), use cloud models where the dust properties do not require the definition of any other additional free parameters other than gravity, effective temperature, and metallicity. Synthetic spectra for a specific set of atmospheric parameters can be compared to empirical spectra. For instance, these models have been tested on spectra of young late-type objects (late-type companions and free-floating objects; Bonnefoy et al. 2010, 2013; Witte et al. 2011; Patience et al. 2012; Manjavacas et al. 2014).

In this paper, we present X-Shooter optical and near-infrared (NIR) spectroscopy of 22 peculiar ultracool dwarfs, with spectral types between L3 and T7. We aim to find unresolved brown dwarf binary systems. Our sample consists of objects with a different spectral classification in the optical and in the NIR or peculiar spectra in comparison with objects of the same spectral type. We want to contribute to the census of unresolved low-mass dwarfs, and at the same time provide new constraints on the BT-Settl 2014 atmospheric models. In Section 2 we describe the procedure for the selection of candidates in our sample, we explain how the observations were performed, and the data reduction procedure. In Section 3 we first perform a search for L+T binaries in our sample, then perform a simulation to estimate the efficiency and false positive rate of the spectral fitting method we apply. We estimate the sensitivity of our method to detect spectral binaries with the same subspectral type. We also compare our targets with trigonometric distances in a colour–magnitude diagram (CMD) with the L, L–T transition, and T brown dwarfs published by Dupuy & Liu (2012). CMD allows us to discover unresolved binaries and young brown dwarfs. In Section 4 we discuss the properties of the binary candidates selected in Section 3. In Section 5 we update the binary sample of very low mass objects.

In Section 6 we investigate how the BT-Settl 2014 atmospheric models reproduce our spectra over the optical and the NIR. We compare with the results from the literature, the equivalent width provided by the models. Finally, in Section 7 we summarize our results.

2 THE SAMPLE, OBSERVATIONS, AND DATA REDUCTION

2.1 Sample selection

We selected a sample of 22 brown dwarfs found in the literature, with optical spectral types between L3 and T7, that have discrepant optical and NIR classification, or peculiar spectra. Optical subtypes are typically earlier than the NIR subtypes. These objects are candidates to be unresolved binaries. We selected the brightest such objects to ensure sufficient SNR in a reasonable integration time ($J < 16$). Furthermore, to calibrate our results and confirm the reliability of our method, we added some known brown dwarfs systems, LHS 102B (Golimowski et al. 2004), formed by an L4.5 plus an L4.5, and SDSS J042348.56−041403.4 (Burgasser et al. 2005), formed by an L6 ± 1 and a T2 ± 1. Our list of targets and their physical properties taken from the literature are compiled in Table 1.

2.2 Observations and data reduction

Our targets were observed using X-Shooter (Wideband ultraviolet–infrared single target spectrograph) on the Very Large Telescope (VLT) between 2009 October and 2010 June. X-Shooter is composed of three arms: UVB (ultraviolet blue, 300–550 nm), VIS (visible, 550–1000 nm) and NIR (near-infrared, 1000–2500 nm). It was operated in echelle slit nod mode, using the 1.6-arcsec slit width for the UVB arm, and the 1.5-arcsec slit width for the optical and the NIR arms. This setup provides resolutions of ∼3300 in the UVB and NIR, and ∼5400 in the VIS. We obtained an average signal-to-noise of ∼30. Observations were performed at the parallactic angle to mitigate the effect of differential chromatic refraction. We moved the object along the slit between two positions following an ABBA pattern with a size of 6 arcsec. The flux expected in the UVB arm is extremely low, therefore we chose not use spectra taken in this range. Telluric standards were observed before or after every target at a close airmass (±0.1 with respect to the targets). Bias, darks, and flats were taken every night. Arc frames were taken every second day. The observing log including telluric standard stars and the raw seeing during the observations is shown in Table A1.

The spectra were reduced using the European Southern Observatory (ESO) X-Shooter pipeline version 1.3.7 (Vernet et al. 2011). In the reduction cascade, the pipeline deletes the non-linear pixels and subtracts bias in the optical or dark frames in the NIR. It generates a guess order from a format-check frame, a reference list of arc line and a reference spectral format table. It refines the guess order table into an order table from an order definition frame obtained by illuminating the X-Shooter pinhole with a continuum lamp. The master flat frame and the order tables tracing the flat edges are created. Finally, the pipeline determines the instrumental response and science data are reduced in slit nodding mode.

In the case of the NIR, we used the spectrum of the telluric star of the corresponding science target observed in the same night to obtain the response function. We removed cosmetics and cosmic rays from the telluric stars, as well as the H and He absorption lines on their spectra, using a Legendre polynomial fit of the pseudo-continuum around the line. We then derived a response function by dividing the non-flux calibrated clean spectrum of the telluric standard by a blackbody synthetic spectrum with the same temperature as the telluric star (Theodossiou & Danezis 1991). Finally, to

Table 1. List of observed targets: magnitudes are in the 2MASS system, except for object Gl 229B for which magnitudes are given by Leggett et al. (1999) in the UKIRT system.

Number	Name	J (mag)	H (mag)	K (mag)	d_{trig} (pc)	SpT OPT	SpT NIR	Remarks	Reference
1	LHS 102B	13.11 ± 0.02	12.06 ± 0.02	11.39 ± 0.02	13.2 ± 0.7	L5	L4.5	Binary	1, 2
2	2MASS J00361617+1821104	12.47 ± 0.02	11.59 ± 0.03	11.31 ± 0.02	8.8 ± 0.1	L3.5	L4	NR[a], V[b]	3, 4, 36
3	2MASS J00531899−3631102	14.45 ± 0.02	13.48 ± 0.03	12.94 ± 0.02		L3.5	L4		5, 6
4	SIMP 01365662+0933473	13.46 ± 0.03	12.77 ± 0.03	12.56 ± 0.02	6.0 ± 0.1		T2.5	V	7, 8
5	2MASS J01443536−0716142	14.19 ± 0.02	13.01 ± 0.02	12.27 ± 0.02		L5		Red	9, 10
6	2MASS J02182913−3133230	14.73 ± 0.04	13.81 ± 0.04	13.15 ± 0.04		L3	L5.5		5,11
7	DENIS-P J0255.0−4700	13.25 ± 0.02	12.20 ± 0.02	11.56 ± 0.02	4.9 ± 0.1	L8	L9	V	12, 13, 35
8	2MASS J02572581−3105523	14.67 ± 0.03	13.52 ± 0.03	12.88 ± 0.03	10.0 ± 0.7	L8	L8.5		4, 5, 14
9	2MASS J03480772−6022270	15.32 ± 0.05	15.56 ± 0.14	15.60 ± 0.02	7.9 ± 0.2		T7		15, 16
10	2MASS J03552337+1133437	14.05 ± 0.02	12.53 ± 0.03	11.53 ± 0.02	9.1 ± 0.1	L5	L3	Y[c]	1, 17, 18, 19, 20, 37
11	SDSS J0423485−041403	14.47 ± 0.02	13.46 ± 0.03	12.93 ± 0.03	15.2 ± 0.4	L7.5	T0	Binary	1, 21, 32, 33
12	2MASS J04390101−2353083	14.41 ± 0.02	13.41 ± 0.02	12.82 ± 0.02	9.1 ± 0.3	L6.5			11, 19
13	2MASS J04532647−1751543	15.14 ± 0.03	14.06 ± 0.03	13.47 ± 0.03		L3pec		Y?	11, 14
14	2MASS J05002100+0330501	13.67 ± 0.02	12.68 ± 0.02	12.06 ± 0.02		L4	L4		1, 22
15	2MASS J05395200−0059019	14.03 ± 0.03	13.10 ± 0.02	12.53 ± 0.02	13.1 ± 0.4	L5	L5	NR	1, 4, 24
16	2MASS J06244595−4521548	14.48 ± 0.02	13.34 ± 0.02	12.59 ± 0.02	11.9 ± 0.6	L5pec	L5		1, 23
17	Gl 229B	13.97 ± 0.03	14.38 ± 0.03	14.55 ± 0.03	5.8 ± 0.4		T7pec	MP[d], Y	33, 34, 35
18	2MASS J10043929−3335189	14.48 ± 0.04	13.49 ± 0.04	12.92 ± 0.02	17.0 ± 1.6	L4	L5		25, 26
19	2MASS J11263991−5003550	14.00 ± 0.03	13.28 ± 0.03	12.83 ± 0.03		L4.5	L6.5	Blue L	27, 28, 29
20	2MASS J13411160−3052505	14.61 ± 0.03	13.72 ± 0.03	13.08 ± 0.02		L2pec	L3		22
21	2MASS J18283572−4849046	15.18 ± 0.05	14.91 ± 0.06	15.18 ± 0.14	11.9 ± 1.1		T5.5		23, 31
22	2MASS J21513839−4853542	15.73 ± 0.07	15.17 ± 0.09	15.43 ± 0.18	16.7 ± 1.1		T4		30

References: 1 – Reid et al. (2008b); 2 – Burgasser et al. (2007); 3 – Dahn et al. (2002); 4 – Schneider et al. (2014); 5 – Marocco et al. (2013); 6 – Martín et al. (2010); 7 – Artigau et al. (2006); 8 – Radigan et al. (2013); 9 – Burgasser, Bardalez-Gagliuffi & Gizis (2011); 10 – Liebert et al. (2003); 11 – Liebert et al. (2003); 12 – Cruz et al. (2003); 13 – Castro et al. (2013); 14 – Kirkpatrick et al. (2008); 15 – Burgasser et al. (2003); 16 – Parker & Tinney (2013); 17 – Cruz, Kirkpatrick & Burgasser (2009); 18 – Allers & Liu (2013); 19 – Faherty et al. (2013); 20 – Gagné et al. (2014); 21 – Antonova et al. (2013); 22 – Antonova et al. (2013); 23 – Faherty et al. (2012); 24 – Leggett et al. (2000); 25 – Andrei et al. (2011); 26 – Gizis (2002); 27 – Folkes et al. (2007); 28 – Faherty et al. (2009); 29 – Burgasser et al. (2008); 30 – Ellis et al. (2005); 31 – Burgasser et al. (2004); 32 – Vrba et al. (2004); 33 – Nakajima et al. (1995); 34 – Oppenheimer et al. (2001); 35 – Costa et al. (2006); 36 – Gelino et al. (2002); 37 – Zapatero Osorio et al. (2014).
Notes. [a]NR: not resolved binary; [b]V: variability found; [c]Y: young; [d]MP: metal poor.

calibrate in response, we used the package *noao.onedspec.telluric* from the software *Image Reduction and Analysis Facility*, (IRAF). More details on data reduction and flux calibration, as well as correction for telluric bands, are described in Alcalá et al. (2014).

To make sure that the flux in the whole NIR spectra was correctly scaled, we calibrated the flux of our NIR spectra using fluxes given by 2MASS (Two Micron All Sky Survey). We convolved our NIR spectra with *J*, *H*, and *K*s filter transmission curves of 2MASS. The resulting spectra were integrated. We calculated the flux for our targets corresponding to the *J*, *H*, and *K*s bands using 2MASS magnitudes (Cohen, Wheaton & Megeath 2003). Finally, we calculated the scaling factor for *J*, *H*, and *K*s bands and multiplied our NIR spectra in *J*, *H*, and *K*s filters to have the same flux as given by 2MASS. We scaled flux from the optical spectra to be consistent with the flux in the NIR. In the overlapping wavelengths of the optical and NIR spectra (995–1020 nm), we calculated a scaling factor, which is the median of the flux in the these wavelengths of the NIR spectra, divided by the median of the flux in the overlapping wavelengths of the optical spectra. The reduced spectra are shown in Fig. B1.[1] Wavelengths affected by telluric absorption are removed from the figure, as well as the optical part for object Gl229B, because it is contaminated by the flux of its companion, and the optical of 2M0144 because it is noisy.

[1] These spectra will be available in the ESO Phase 3 data release.

3 SEARCH FOR SPECTRAL BINARIES

In this section, we used different methods to reveal unresolved brown dwarf binaries through their spectra. These methods are tailored to the type of brown dwarf binaries that we aim to find.

3.1 Finding L plus T brown dwarf binaries

The combined spectra of L plus T brown dwarf binary systems are predicted to show peculiar characteristics. Those spectra are expected to have blended atomic and molecular absorptions of L and T brown dwarf spectra. This combination may result in a peculiar spectrum. Burgasser et al. (2007, 2010) and Bardalez Gagliuffi et al. (2014) have studied the spectral characteristics of L plus T brown dwarf binary spectra and they have designed an empirical method to identify them using spectroscopy.

Spectra of L plus T binary systems show bluer spectral energy distribution in the NIR than single objects of the same spectral type (Burgasser et al. 2010). Some spectral features vary: the CH_4 and H_2O features at 1.1 μm are deeper for binaries. The CH_4 feature at 1.6 μm is stronger in comparison to the 2.2 μm CH_4 band. At 2.1 μm the flux peak is shifted to the blue for the binaries. They also show larger flux from the T dwarf at 1.55 μm (Bardalez Gagliuffi et al. 2014). Using such differences, Burgasser et al. (2006, 2010) and Bardalez Gagliuffi et al. (2014) defined spectral indices to identify L plus T brown dwarf binary candidates. Typically, spectral indices are defined as the ratio of spectral flux in two different wavelength intervals. The indices are specified in Table C1. Burgasser et al.

Table 2. Candidates selected by Burgasser et al. (2006, 2010) and Bardalez Gagliuffi et al. (2014) indices.

Number	Candidate	Number of satisfied criteria from Burgasser et al. (2006, 2010)	Type of candidate	Number of satisfied criteria from Bardalez Gagliuffi et al. (2014)	Type of candidate
3	2M0053	2	Weak candidate	6	Weak candidate
4	SIMP01365	4	Strong candidate	8	Strong candidate
7	DE0255	2	Weak candidate	7	Weak candidate
8	2M0257	2	Weak candidate	6	Weak candidate
11	SD0423	2	Weak candidate	7	Weak candidate
20	2M1341	2	Weak candidate	8	Strong candidate

(2006, 2010) and Bardalez Gagliuffi et al. (2014) compared all indices against each other for a large sample of brown dwarfs, some of them L plus T known binaries. They identified the best pairs of indices that segregated known binaries from the rest of the objects, and selected the regions in each combination of indices that delimit the known L plus T known binaries. In Tables C2 and C3 these regions are defined. There are several differences between Burgasser et al. (2006, 2010) and Bardalez Gagliuffi et al. (2014) methods. Burgasser et al. (2006, 2010) published eight indices that are valid only to find L plus T dwarf binaries, and defined six binary index selection criteria. The objects that satisfied two criteria were considered as 'weak candidates'. Those that satisfied three or more criteria are considered 'strong candidates'. Bardalez Gagliuffi et al. (2014) used the eight spectral indices defined in Burgasser et al. (2006, 2010) and developed five new indices that are sensitive to M7–L7 plus T binaries. Bardalez Gagliuffi et al. (2014) defined 12 new binary selection criteria. Objects satisfying four to eight criteria were considered as 'weak candidates'. Those that satisfied more than eight indices were considered 'strong candidates'.

By calculating these spectral indices we selected those objects in our sample that are L plus T binary candidates. The result using Burgasser et al. (2006, 2010) criteria is shown in Fig. C1, and the result using Bardalez Gagliuffi et al. (2014) criteria is shown in Figs C2 and C3. In Table 2, we summarize the weak and strong candidates given by each method.

To confirm or reject the selected L plus T binary candidates, we compared our spectra with libraries of well-characterized brown dwarf spectra, i.e. template spectra. We used as template spectra the McLean et al. (2003) and Cushing, Rayner & Vacca (2005) libraries, with a resolution of $R \sim 2000$, as well as the SpeX Prism Spectral Library spectra,[2] with a resolution of $R \sim 120$. In total we considered 462 spectra from SpeX Spectral Library plus 14 from Cushing et al. (2005) library and 47 spectra from McLean et al. (2003) library, with spectral types from L0 to T7.

We degraded the resolution of our X-Shooter spectra to the resolution of each template. We re-interpolated the library of brown dwarf template spectra and X-Shooter spectra to the same grid. We searched for the best matches to template spectra of single objects from SpeX, Cushing et al. (2005), and McLean et al. (2003) libraries, and synthetic binary spectra created using those libraries. To create those synthetic binaries, we calibrated the fluxes of the components to the same distance using an absolute magnitude–colour relation (Dupuy & Liu 2012) and add them together. The final resolution of our synthetic binary templates was the same as the SpeX spectral library spectra.

To identify the best matches to our spectra, we used the approach explained in Cushing et al. (2008), which is similar[3] to a χ^2,

$$G = \sum_{\lambda} \boldsymbol{w}(\boldsymbol{\lambda}) \left[\frac{C(\lambda) - \alpha T(\lambda)}{\sigma_c(\lambda)} \right]^2, \quad (1)$$

where $C(\lambda)$ is the spectrum of the candidate, $T(\lambda)$ is the template spectrum, $\boldsymbol{w}(\boldsymbol{\lambda})$ is a vector of weights proportional to the waveband size of each pixel, α is a scaling factor that minimizes G, and $\sigma_c(\lambda)$ are the errors of the spectrum. To calculate the G, we used the parts of the spectra where no strong telluric absorptions are contributing, since we are confident of the telluric correction resulting from the data reduction process: $\lambda = 950$–1350, 1450–1800, and 2000–2350 nm. We additionally checked the best matches by visual inspection. Finally, we tested if the fit to a binary template was significantly better than the fit to a single template using a one-sided F-test statistic. We used as the distribution statistic ratio

$$\eta_{\rm SB} = \frac{\min(G_{\rm single})\mathrm{df}_{\rm binary}}{\min(G_{\rm binary})\mathrm{df}_{\rm single}}, \quad (2)$$

where $\min(G_{\rm single})$ and $\min(G_{\rm binary})$ are the minimum G for the best match to a single or to a composite template, and $\mathrm{df}_{\rm binary}$ and $\mathrm{df}_{\rm single}$ are the degrees of freedom for the binary template fit and the single template fit. The degrees of freedom are the number of data points used in the fit ($n = 296$) minus 1 to account the scaling between our spectra and the template spectra. To rule out the null hypothesis, meaning that the candidate is not a binary with a 99 per cent confidence level, we require $\eta_{\rm SB} > 1.31$.[4] The F-test analysis rejected three of our candidates, namely SIMP0136, 2M0257, and 2M1341.

In Table 3 we show the best matches of the selected candidates to single and composite brown dwarf spectra. Plots with the best matches are shown in Appendix D.

We intended to estimate the fraction of missed L plus T binaries applying Burgasser et al. (2007, 2010) and Bardalez Gagliuffi et al. (2014) method. To this aim, we compared 47 synthetic L plus T binaries to single L dwarfs, single T dwarfs and to other synthetic L plus T binaries. We found that 21 per cent of the L plus T synthetic

[2] The SpeX Prism Spectral Library is maintained by C. Gelino, D. Kirkpatrick, M. Cushing, D. Kinder and A. Burgasser: http://pono.ucsd.edu/~adam/browndwarfs/spexprism/

[3] G is mathematically similar to a χ^2, but it does not follow a χ^2 distribution as our comparison spectra have noise (see Cushing et al. 2008 for further details). We therefore do not expect to achieve $G \sim 1$ for the best fits; our goal is to determine whether a binary template is fitting better than a single template for our selected binary candidates.

[4] Burgasser et al. (2006, 2010) require a confidence level of 99 per cent, and Bardalez Gagliuffi et al. (2014) a confidence level of 90 per cent. We employed a confidence level of 99 per cent to be more conservative, and minimize the false positives rate.

Table 3. Best matches to objects selected as binary candidates by spectral indices.

Candidate	Single best match spectrum	Composite best match spectrum	η_{SB}	Fig.
2M0053	2MASS J17461199+5034036 (L5)	Kelu-1 (L3p) + SDSS J120602+281328 (T3)	1.35	D1
SIMP01365	SDSS J152103.24+013142 (T2)	DENIS-PJ225210−173013 (L7.5, bin) + SDSS J000013+255418 (T4.5)	0.55	D2
DE0255	SDSS J085234.90+472035.0 (L9.5)	SDSS J163030.53+434404.0 (L7) + SDSS J103931.35+325625.5 (T1)	3.42	D3
2M0257	SDSS J104409.43+042937.6 (L7)	2MASS J0028208+224905 (L7) + SDSS J204749.61−071818.3 (T0)	1.23	D4
SD0423	SDSS J105213.51+442255.7 (T0.5)	2MASS J15150083+4847416 (L6) + SDSS J125453.90−012247.4 (T2)	3.23	D5
2M1341	GJ1048B (L1)	GJ1048B (L1) + 2MASS J1217110−031113 (T7.5)	1.26	D6

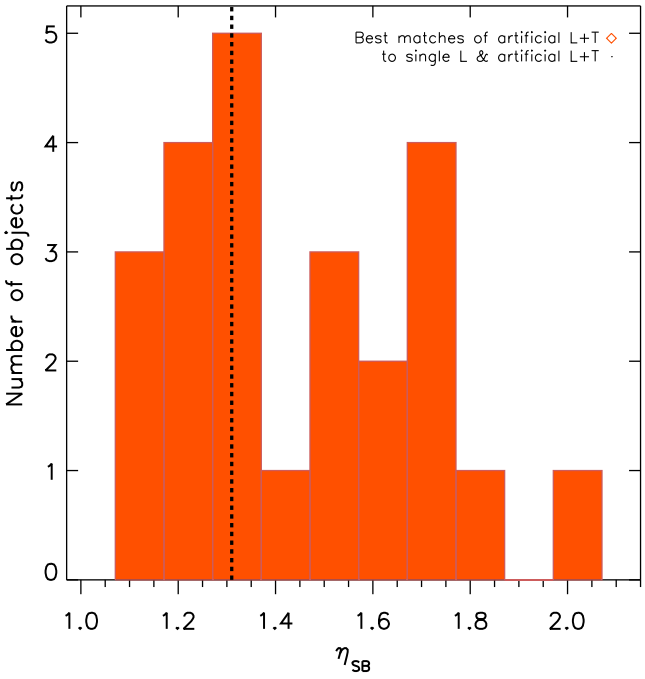

Figure 1. Histograms of η_{SB} for comparison of L plus T synthetic brown dwarf spectra to single L and other synthetic L+T brown dwarfs spectra. The dashed black line indicates $\eta_{SB} = 1.31$.

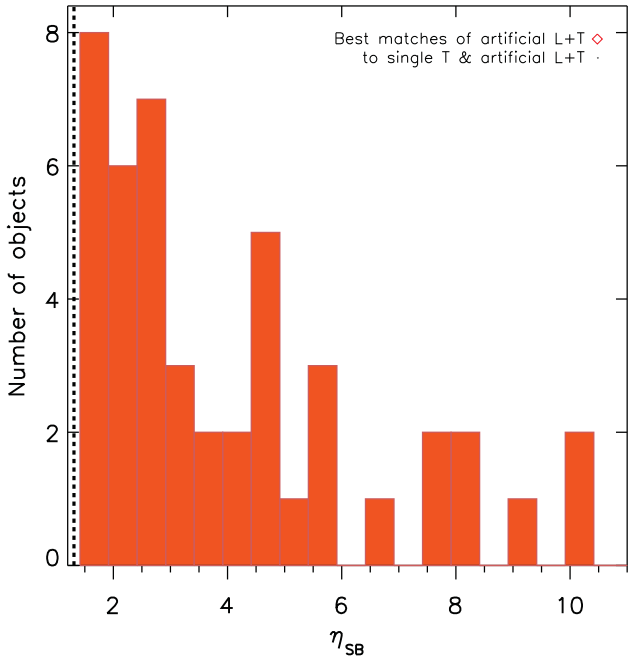

Figure 2. Histograms of η_{SB} for comparison of L plus T synthetic brown dwarf spectra to single T spectra and other synthetic L+T spectra. The dashed black line indicates $\eta_{SB} = 1.31$.

binaries, did not satisfy the binarity condition (i.e. they had $\eta_{SB} < 1.31$). In particular, for 10 L plus T artificial binaries the match to single L dwarfs was significantly better than with binaries (see Fig. 1). In Fig. 2, for all L plus T synthetic systems the binarity criteria was satisfied. Therefore, most of the L plus T systems should be found using this method, but it must be taken into account that some binaries might be lost.

Finally, we compared a sample of 43 single L dwarfs to other L single dwarfs, and to synthetic L plus T binaries (see Fig. 3). We found that 37 per cent of the single L dwarfs satisfied the binarity criteria, i.e. they had significantly better matches with L plus T synthetic binaries, they are therefore false positives. Equally, we performed a similar analysis for a sample of 40 single T dwarfs. We obtained that 35 per cent of the T dwarfs are also false positives (see Fig. 4). We examined the spectral characteristics reported in the literature for the subsamples of 16 L dwarfs and 14 T dwarfs with best matches to synthetic L plus T binaries. We found that 5 of the 16 L dwarfs, and 2 of the 14 T dwarfs had either peculiar spectra or different spectral classification in the optical and the NIR. The conclusions of this analysis are summarized in Table 4. These results suggest that this method is efficient finding different spectral type binaries, but it should be applied with caution, as some false positives might be found.

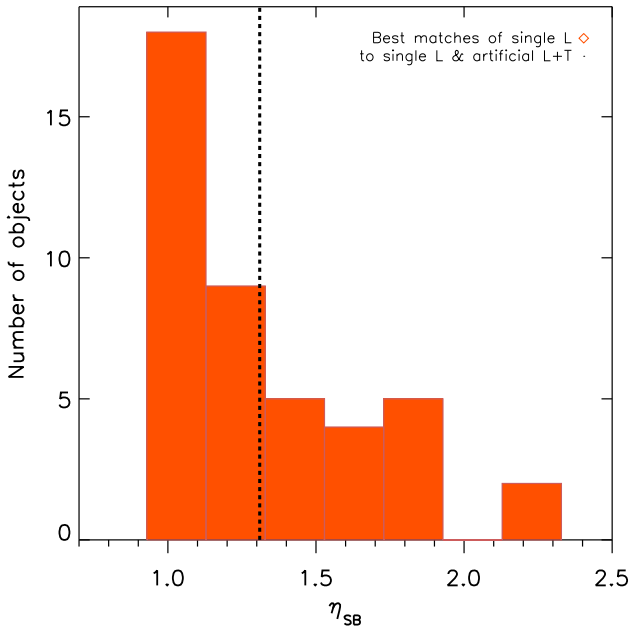

Figure 3. Histograms of η_{SB} for comparison of L single brown dwarf spectra to other L single dwarfs and synthetic L+T brown dwarfs spectra. The dashed black line indicates $\eta_{SB} = 1.31$.

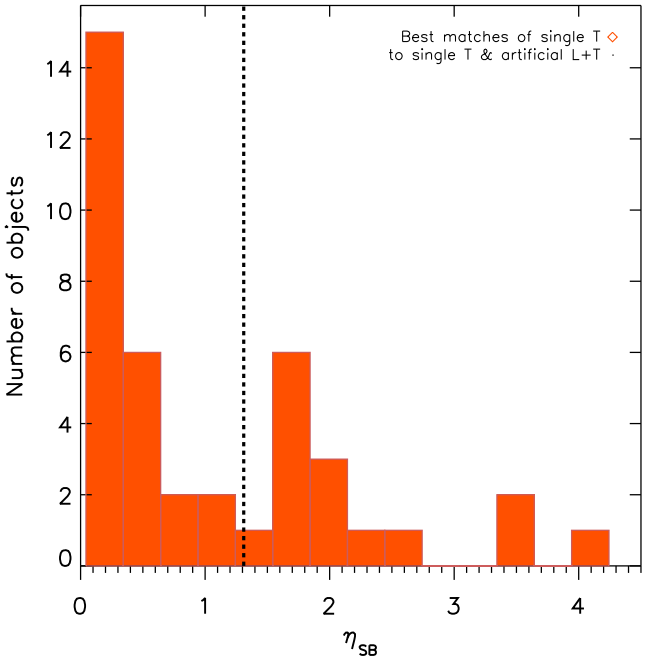

Figure 4. Histograms of η_{SB} for comparison of T single brown dwarf spectra to other single T dwarfs and synthetic L+T brown dwarfs spectra. The dashed black line indicates $\eta_{SB} = 1.31$.

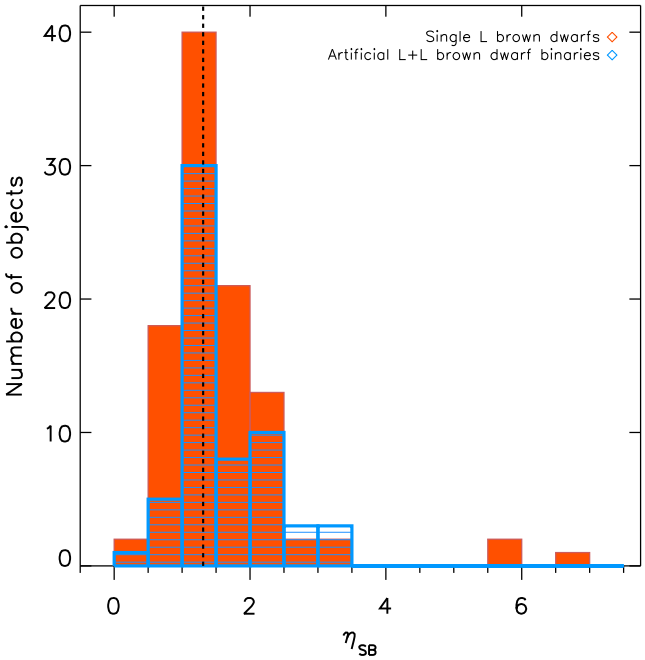

Figure 5. Histograms of η_{SB} for comparisons of single L brown dwarfs (in red) and artificial L plus L binaries (blue with lines), to other single L dwarfs and other L plus L synthetic binaries. The dashed black line indicates $\eta_{SB} = 1.31$.

3.2 Finding equal spectral type brown dwarf binaries

We aimed to find equal spectral type brown dwarf binaries comparing to spectral templates. To this purpose, we have chosen 101 L0–L9 presumed single brown dwarfs spectra from the SpeX library. Additionally, we have created 60 synthetic brown dwarf binaries in which both components have similar spectral type, i.e. the same spectral type, but different spectral subtypes. To create those, we chose several presumed single L brown dwarfs from the SpeX sample, and we created synthetic binary spectra combining single brown dwarf spectra following the same procedure as in Section 3.1.

We compared the 101 single L dwarfs and the 60 artificial L plus L dwarf binaries to other L single SpeX spectra, and to other synthetic L binaries. We determined the best match of the 101 single L and the 60 synthetic L plus L binaries calculating the *G* parameter as in equation (1), and we equally decided the significance of the best match using equation (2). We made a similar analysis for 56 T single dwarfs, and 74 T plus T synthetic binaries.

We compared the best matches to single L and T dwarf spectra, and the best matches to synthetic binaries with similar spectral type (L plus L and T plus T, respectively). To this aim, we calculated the η_{SB} parameter for the 101 single L dwarfs, 56 single T, and for the 60 L plus L and 63 T plus T artificial binaries created. In Figs 5 and 6, we represent in a red histogram single brown dwarfs, and artificial dwarf binaries in a blue histogram with horizontal lines.

We found that 49 per cent of the 101 L single dwarfs, and 62 per cent of the 60 synthetic L binaries, satisfied the binarity criteria. In Fig. 5, we show that the distribution of η_{SB} for single L and for synthetic L plus L binaries is similar.

Equally, we performed a similar simulation for T dwarfs. We found that 57 per cent of the 56 T single dwarfs, and 86 per cent of the 56 T plus T synthetic binaries satisfied the binarity criteria. In Fig. 6, we show the distributions of η_{SB} for single T and for synthetic T plus T binaries.

For the cases mentioned before, the distribution of the η_{SB} value is the same for single and synthetic binaries with the same spectral types, but different subspectral types. Therefore, it is impossible to distinguish between single L or T dwarfs and synthetic L or T dwarf binaries. Furthermore, for both cases, the best fits are usually other synthetic binary spectra. These results are summarized in Table 5. Additional data, such as parallax measurements, high-resolution imaging or high-resolution spectra are necessary in order to find these systems.

Table 4. Summary of the results obtained from Figs 1–4.

Type of objects	First comparison objects	Second comparison objects	Best matches	Fig.
Synthetic L+T binaries	Single L dwarfs	Synthetic L+T binaries	21 per cent to single L dwarfs (false negatives) 79 per cent to L+T synthetic binaries	1
Synthetic L+T binaries	Single T dwarfs	Synthetic L+T binaries	0 per cent to single T dwarfs 100 per cent to L+T synthetic binaries	2
Single L dwarfs	Single L dwarfs	Synthetic L+T binaries	63 per cent to single L dwarfs 37 per cent to L+T syntetic binaries (false positives)	3
Single T dwarfs	Single T dwarfs	Synthetic L+T binaries	65 per cent to single T dwarfs 35 per cent L+T synthetic binaries (false positives)	4

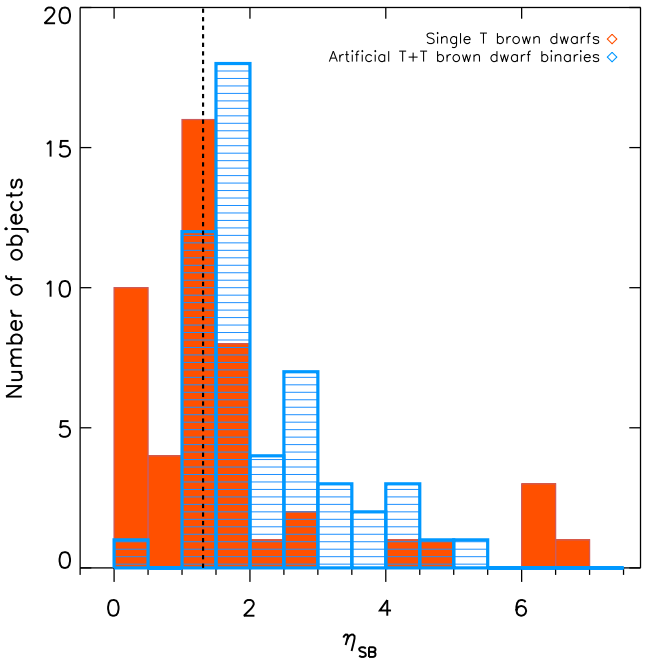

Figure 6. Histograms of η_{SB} for comparisons of single T brown dwarfs (in red) and artificial T plus T binaries (blue with lines), to other single T dwarfs and other T plus T synthetic binaries. The dashed black line indicates $\eta_{SB} = 1.31$.

3.3 Photometric search for brown dwarf binaries

In our 22 object sample, distances for 15 objects are available in the literature, with a precision of 10 per cent or better. In Fig. 7 we present a CMD showing the $J - K$ colour in the MKO (Mauna Kea Observatory) photometric system versus absolute magnitude in the J band. In this figure, we plot all brown dwarfs with known parallaxes (Dupuy & Liu 2012), the 15 objects of our sample with known parallaxes, and the colour–absolute magnitude relationship by Dupuy & Liu (2012). The two known binaries in our sample (LHS102B and SD0423, targets 1 and 11, respectively) stand out over objects with their same spectral types and other one, the young object 2M0355 (target 10) is much redder as objects of its same spectral type because of its youth. For the rest of the objects we cannot draw clear conclusions as there are no clear outliers.

4 INDIVIDUAL CANDIDATES

Six objects in our sample were selected as binary candidates by spectral indices. After fitting, three of our candidates were rejected due to the confidence level being lower than 99 per cent. This leads to a final number of three selected candidates.

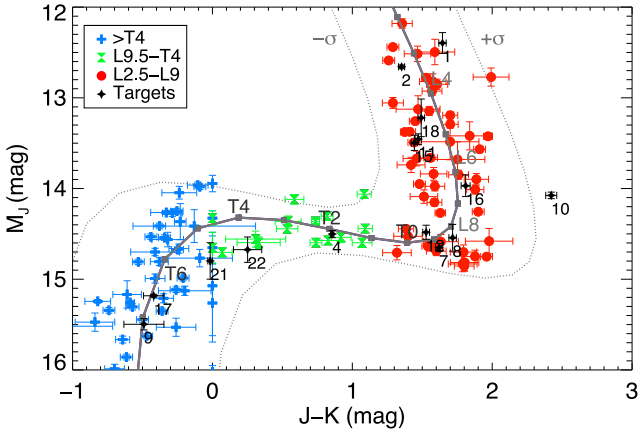

Figure 7. Colour–magnitude diagram in the MKO system showing brown dwarfs with measured parallaxes from (Dupuy & Liu 2012), and its colour–absolute magnitude relationship together with its plus minus 1σ curves (dotted line). Our targets are shown in black. Objects have the same numbers as in Table 1.

One of our selected candidates, the confirmed binary SD0423, was studied by Burgasser et al. (2005) and was used as a test of consistency of the spectroscopic method by Burgasser et al. (2010). We do not discuss it here.

4.1 Rejected candidates

We do not consider the following targets as a binary candidate in the rest of the paper.

4.1.1 SIMP 01365662+0933473

SIMP 0136 was discovered by Artigau et al. (2006) and classified as a T2.5. Goldman et al. (2008) searched for companions using NACO/VLT, reaching a sensitivity of 0.2 arcsec (1–40 au), but no companions were found. Artigau et al. (2009) detected photometric variability in the J and K bands with a modulation of ∼2.4 h and an amplitude of 50 mmag. Radigan et al. (2012) calculated the amplitude of the variability for an object similar to SIMP 0136 (2MASS J21392676+0220226, T1.5). If this variability were produced by a companion, it would be much smaller than the variability obtained. Therefore, we do not expect that it is caused by a companion. Apai et al. (2013) explained it as a mixture of thick and thin patchy iron and silicate clouds covering the surface of the object.

The object SIMP 0136 was selected as a brown dwarf binary candidate, but it was rejected by an F-statistic analysis in Section 3.1. Spectral indices used in Section 3.1 are suitable to select peculiar spectral characteristics that appear usually in binary L plus T brown dwarf spectra. However, if variability is produced

Table 5. Summary of the results obtained from Figs 5 and 6.

Type of objects	First comparison objects	Second comparison objects	Best matches	Fig.
Single L dwarfs	Single L dwarfs	Synthetic L+L binaries	51 per cent single L dwarfs 49 per cent L+L syntetic binaries (false positives)	5
Synthetic L+L binaries	Single L dwarfs	Synthetic L+L binaries	38 per cent single L dwarfs (false negatives) 62 per cent L+L synthetic binaries	5
Single T dwarfs	Single T dwarfs	Synthetic T+T binaries	43 per cent single T dwarfs 57 per cent T+T synthetic binaries (false positives)	6
Synthetic T+T binaries	Single T dwarfs	Synthetic T+T binaries	12 per cent single T dwarfs (false negatives) 86 per cent T+T synthetic binaries	6

by a partial coverage of thick and thin clouds in the brown dwarf atmosphere, similar peculiar spectral characteristics would appear in brown dwarf spectra.

A preliminary parallax of 166.2 ± 2.9 mas for SIMP 0136 was obtained from the NPARSEC programme (ESO programme 186.C-0756; Smart et al. 2013). Using this parallax, we placed the object in a CMD together with other L, L–T transition, and T brown dwarfs with parallaxes (Dupuy & Liu 2012), as shown in Fig. 7. We compared SIMP 0136 to objects of similar spectral type. We did not find significant overluminosity, expected in the case of late-L and early-T brown dwarf binaries. This result is compatible with the rejected binary hypothesis by the F-test.

4.1.2 2MASS J02572581−3105523

The target 2M0257 was discovered by Reid et al. (2008b). Kirkpatrick et al. (2008) classified it as an L8 in the optical. Marocco et al. (2013) measured its trigonometric parallax to be $\pi = 99.7 \pm 6.7$ mas. It was selected by spectral indices as a weak brown dwarf binary candidate, and it was rejected by the F-statistic.

When we compared this target with objects of similar spectral type in the CMD, no overluminosity was found. This result agrees with the non-binarity scenario.

4.1.3 2MASS J13411160−3052505

The target 2M1341 was discovered by Reid et al. (2008a). Faherty et al. (2009) published a distance of 24 ± 2 pc. Kirkpatrick et al. (2011) classified it as a peculiar L2. Bardalez Gagliuffi et al. (2014) compared it to several SpeX templates and concluded that this object could be a L1.2 ± 0.3 plus a T6.3 ± 1.0.

In Section 3.1, target 2M1341 was selected as a weak candidate L plus T binary by Burgasser et al. (2006, 2010) indices, but it was selected as a strong candidate by Bardalez Gagliuffi et al. (2014) indices. This candidate was rejected by our conservative F-test criterion. However, a detailed inspection of the observed spectroscopic matches (see Fig. D6) reveals no satisfactory reproduction of the NIR features, thus leaving open the multiplicity of 2M1341. High-resolution observations are required to disentangle its true nature.

4.2 Selected candidates

4.2.1 2MASS J00531899−3631102

The object 2M0053 was discovered by Reid et al. (2008b). Kirkpatrick et al. (2008) classified it as an L3.5 in the optical. It was selected as a weak brown dwarf binary candidate. We found a best match with a combination of a L3 dwarf and a T3 dwarf. There is no parallax measurement available for this target.

4.2.2 DENIS-P J0255.0−4700

The target DE0255 was discovered by Martín et al. (1999) and it was classified as a peculiar L6. Koen et al. (2005) reported evidence of variability in different time-scales (1.7 and 5 h). Morales-Calderón et al. (2006) concluded that DE0255 may vary with a 7.4 h period at 4.5 μm, but it does not at 8 μm. Costa et al. (2006) reported an absolute parallax of $\pi = 201.4 \pm 3.9$ mas. Burgasser et al. (2008) classified it in the optical as an L8 and in the NIR as an L9. Finally, Reid et al. (2008a) searched for multiplicity for this target using high-resolution NICMOS NIC1 camera imaging on the *Hubble Space Telescope*, but found no evidence of multiplicity.

In Section 3.1, DE0255 was selected as an L plus T weak binary candidate. We found a best match for DE0255 to a composite spectra of an L7 plus T1 spectra (see Fig. D3).

Using the Costa et al. (2006) published parallax, we plot DE0255 in a CMD as above (see Fig. 7). In the case of a late-L and early-T binary scenario, we expect to find about ∼0.5 mag overluminosity comparing with objects of similar spectral type on a CMD. In this case, no overluminosity was found, weakening the binarity hypothesis for object DE0255.

5 VERY LOW MASS BINARY FRACTION

In our peculiar sample of 22 objects, we found three L+T binary candidates. One of them has been confirmed by other authors using high-resolution imaging (SD0423, by Burgasser et al. 2005). Other two objects were selected as weak binary candidates (2M0053 and DE0255). The binarity hypothesis is weakened for object DE0255, due to the lack of overluminosity in the CMD (see Fig. 7), expected for late-L and early-T brown dwarf binary scenario.

This result allowed us to estimate the minimum and the maximum L+T binary fraction for our sample, and samples selected using our same criteria (see Section 2). The minimum L+T binary fraction[5] is estimated at $4.5^{+9.1}_{-1.4}$ per cent (the only confirmed L+T binary is SD0423 over the whole 22 targets sample). The L+T maximum binary fraction for our sample is estimated at $13.6^{+10.4}_{-4.3}$ per cent (the three L+T binary candidates over the whole 22 targets sample). These pairs would have a mass ratio of $q \geq 0.5$ for ages between 1 and 5 Gyr (expected for most of the objects in this study). Our work is not sensitive to smaller mass ratios. The derived range for the L+T binarity coincides with the fraction of late-M stars of the solar neighbourhood that host T-type companions. As summarized by Burgasser et al. (2015), there are two late-M stars with T-type brown dwarf companions, among 14 dwarfs with spectral types between M7 and M9.5, and at 10 pc from the Sun (∼14 per cent). Therefore, it appears that the L dwarf primaries have T-type companions with a similar frequency to the late-M objects, despite the fact that the former primaries are expected to be less massive than the latter for typical field ages.

Regarding binaries that include L+L and T+T pairs in our sample, there is just one confirmed L4.5+L4.5 system in our target list (LHS 102B). LHS 102B cannot be detected using the methods we employed in this paper, given the limitations of the spectroscopic technique.

We thus determined the minimum fraction of L+L, T+T, and L+T pairs for our sample to be $9.1^{+9.9}_{-3.0}$ per cent (the confirmed brown dwarf binaries, SD0423 and LHS102B over the whole sample of 22 objects). In spite of the peculiarity of our sample, this lower limit agrees with other values reported previously by different groups (Burgasser 2007; Goldman et al. 2008; Bardalez Gagliuffi et al. 2014; Burgasser et al. 2015).

6 COMPARISON TO THE BT-SETTL ATMOSPHERIC MODELS

The X-Shooter spectra presented in this paper provide the possibility to compare with the BT-Settl atmospheric models in a wide range of wavelengths (550–2500 nm). We used 13 objects of our total sample to test the BT-Settl models 2014. We excluded brown dwarf

[5] The uncertainties of the binarity fraction for samples with less than 100 objects are calculated using the method explained in Burgasser et al. (2003).

binary candidates and spectra with low signal-to-noise to avoid false results.

The BT-Settl models account for the formation and gravitational settling of dust grains for an effective temperature ($T_{\rm eff}$) below ≈2700 K in the photosphere of the objects, following the approach described in Rossow (1978). The models include 180 types of condensates via their interaction with the gas phase chemistry, depleting the gas from their vapour phase counterparts. 55 of these grain species are included in the radiative transfer calculations to the extent to which they have not settled from the cloud layer. Log-normal grain size distributions with a standard deviation of 1 are used, where the characteristic grain size for each layer is determined from the equilibrium size derived by the cloud model. The original time-scales approach of the Rossow (1978) model has further been extended to account for nucleation as an additional time-scale, which is defined by assuming a fixed seed formation rate motivated by studies of cosmic ray interactions with the Earth atmosphere (Tanaka 2005).

The cloud model is implemented in the PHOENIX multipurpose atmosphere code version 15.5 (Allard et al. 2001), which is used to compute the model atmospheres and to generate synthetic spectra. Convective energy transport and velocities are calculated using mixing length theory with a mixing length of 1.6–2.0 pressure scaleheights, depending on surface gravity (log g), and overshoot is treated as an exponential velocity field with a scaleheight based on the RHD simulations of Ludwig, Allard & Hauschildt (2002, 2006) and Freytag et al. (2010, 2012); an additional advective mixing term due to gravity waves is included as described in Freytag et al. (2010). All relevant molecular absorbers are treated with line-by-line opacities in direct opacity sampling as in Allard et al. (2003b); regarding this, the molecular line lists have been updated as follows: water-vapour (BT2; Barber et al. 2006), vanadium oxide from Plez (2004, private communication), TiO line list from Plez (2008), and collision-induced absorptions of H_2 (Abel et al. 2011). Non-equilibrium chemistry for CO, CH_4, CO_2, N_2, and NH_3 is treated with height-dependent diffusivity also based on the RHD simulation results of Freytag et al. (2010).

6.1 Comparison to synthetic spectra

In this section, we compared X-Shooter optical and NIR spectra to predictions of the last version of the BT-Settl atmospheric models (Allard et al. 2003a, 2007; Allard, Homeier & Freytag 2011) of 2014. We exclude brown dwarf binary candidates and spectra with low signal-to-noise. We derive atmospheric parameters of the objects and to reveal non-reproducibilities of the models. The models are described in Allard et al. (2011, 2012a,b).

We selected subgrids of synthetic spectra with 400 K ≤ $T_{\rm eff}$ ≤ 2100 K, 3.5 ≤ log g ≤ 5.5 and metallicities of +0.0 and +0.3, which are the metallicities for which the latest version of the BT-Settl models are available. The solar metallicity is based on metallicities calculated by Caffau et al. (2011). The spacing of the model grid is 50 K and 0.5 dex in log g. Effective temperature, gravity, metallicity, and alpha element enhancement are described in the model name strings as `lte-LOGG+[M/H]a+[ALPHA/H]`.

The BT-Settl 2014 synthetic spectra were smoothed to the resolution of X-Shooter. The models were then reinterpolated on the X-Shooter wavelength grid. The spectra were normalized using the same method as in Section 3 and explained in Cushing et al. (2008). The results from the fit were always double checked visually. The atmospheric parameters corresponding to the best-fitting models are reported in Table 6. The parameters $T_{\rm eff}$, log g, and [M/H] have uncertainties of 50 K, and 0.5 dex, respectively. These errors correspond to the sampling of the atmospheric parameters of the model grids. We avoid the following objects to test models: binary candidates (2M1341, DE0255, SIMP0136, 2M0053, 2M0257), known binaries (LHS102B, SD0423), noisy spectra (2M0144), or targets with known nearby objects that may contaminate the spectra, like in the case of Gl229B.

Table 6. Atmospheric parameters corresponding to the best-fitting spectra or synthetic fluxes for our targets. We give $T_{\rm eff}$/log g/[M/H].

Name	$T_{\rm eff}$	log g	[M/H]
2MASS J00361617+1821104	1800	5.5	+0.0
2MASS J02182913−3133230	1800	5.0	+0.3
2MASS J03480772−6022270	950	5.0	+0.0
2MASS J03552337+1133437	1700	4.0	+0.3
2MASS J04390101−2353083	1800	5.0	+0.3
2MASS J04532647−1751543	1750	5.5	+0.0
2MASS J05002100+0330501	1800	5.0	+0.3
2MASS J05395200−0059019	1800	5.5	+0.0
2MASS J06244595−4521548	1700	4.5	+0.3
2MASS J10043929−3335189	1800	5.0	+0.3
2MASS J11263991−5003550	1900	5.5	+0.0
2MASS J18283572−4849046	1100	5.5	+0.0
2MASS J21513839−4853542	1100	5.0	+0.0

Notes. The grid size in $T_{\rm eff}$ is 50 K and in log g is 0.5 dex. Uncertainties in $T_{\rm eff}$ and log g are the same as the grid sizes for both parameters.

The CH_4 and the FeH molecules opacities are still incomplete in the new BT-Settl 2014 models. Methane line opacities are based on the semi-empirical list of Homeier, Hauschildt & Allard (2003), which is highly incomplete in the H band and only supplemented with a small set of room-temperature transitions for the Y and J bands. Iron hydride causes absorption features through the $F\,^4\Delta$–$X\,^4\Delta$ system between 650 and 1600 nm, but in addition to this Hargreaves et al. (2010) identified significant opacity contributions from the $A\,^4\Pi$–$A\,^4\Pi$ system, which is not yet included in the list of FeH lines available to PHOENIX. This explains that the H band is not well reproduced for any of the L or T brown dwarf spectra, and also the J band in the case of T brown dwarfs. For three of the L brown dwarfs, the best match is found for log g = 5.5, with solar metallicity, four of the L brown dwarfs have best matches with log g = 5.0, but [M/H] = +0.3.

Best matches to the BT-Setll models are shown in Figs E1 and E2. There are two of the L brown dwarfs that have best matches with low-gravity models, 2M0355 and 2M0624. Object 2M0355 is known previously to be young (Allers & Liu 2007; Cruz et al. 2009; Zapatero Osorio et al. 2014), so we expect gravity to be lower. The result given by the models is consistent with the literature. There are no references of youth for object 2M0624. Furthermore, the target does not show extremely redder $J-K$ colour in Fig. 7 or significantly weaker alkali lines on Figs 8 and 9, as low-gravity objects do. Best matches to T-type brown dwarfs are always solar metallicity models. The best match to object 2M1828 is to a model with high gravity.

6.2 Comparing predicted and observed equivalent widths

We measured the equivalent width of a variety of alkali lines with sufficient signal-to-noise in our spectra and we compared those values to predictions of the BT-Settl 2014 models. In the optical, we measured the equivalent width of the Rb I (794.8 nm),

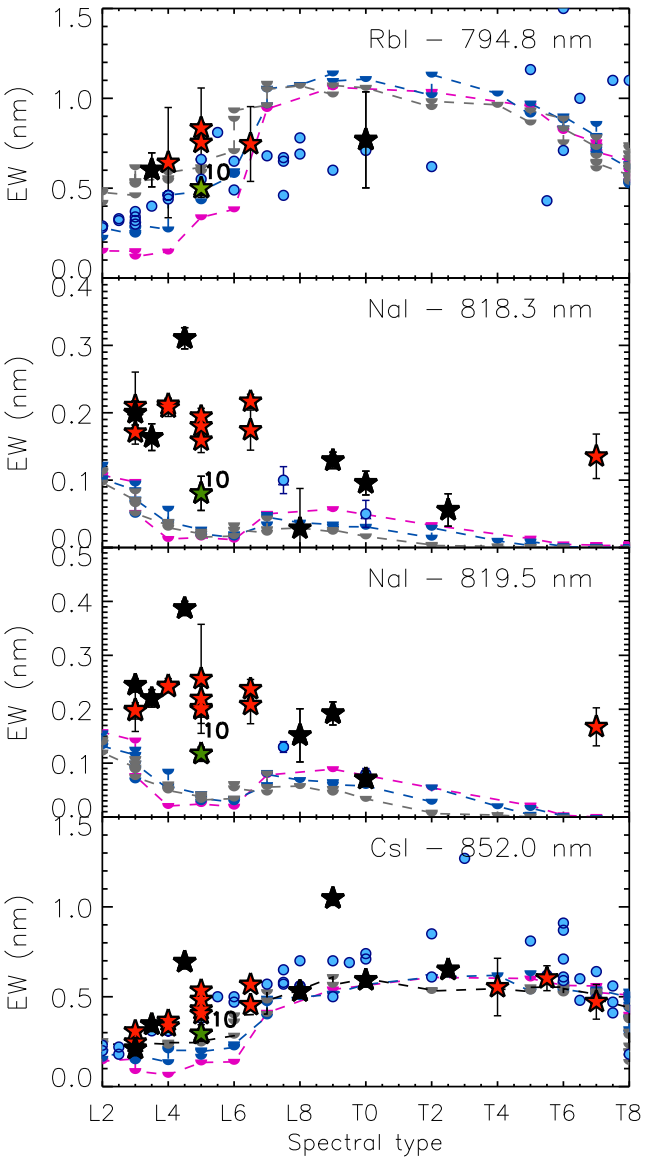

Figure 8. Equivalent widths of the detected alkali lines in the optical for our targets (red stars), binary candidates or known binaries from our sample (black stars), and for objects with equivalent width available in the literature (blue circles). The young object 2M0355 (number 10) is marked as green star. These equivalent widths come from Chiu et al. (2006), Golimowski et al. (2004), Knapp et al. (2004), and Lodieu et al. (2015). We overplot with coloured half circles joined by coloured dashed lines the EW predicted by the BT-Settl models 2014 for different gravities. The pink half-filled circles and dashes lines correspond to log $g = 4$, the blue ones correspond to log $g = 4.5$, and the grey ones to log $g = 5.0$.

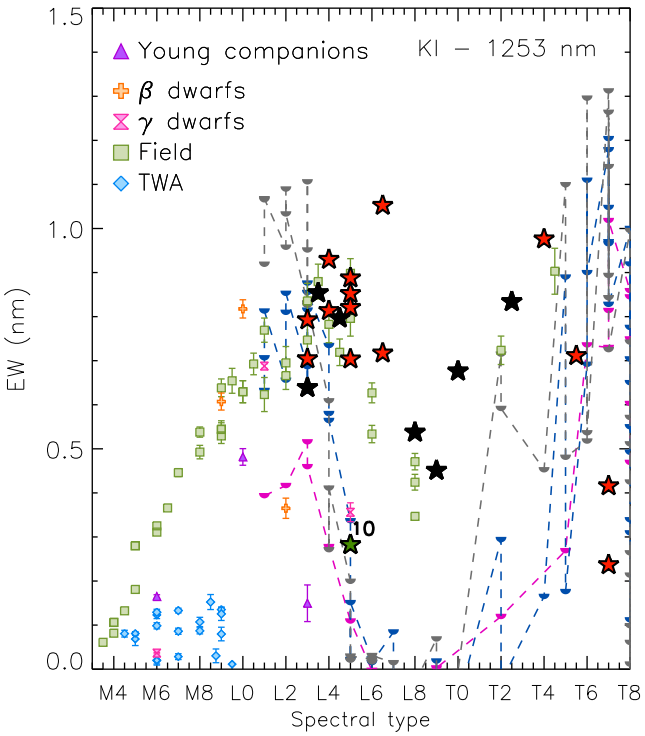

Figure 9. Equivalent widths of the K I alkali line at 1253 nm of our objects (red stars), and binary candidates or known binaries of our sample (black stars), compared to the equivalent widths of field brown dwarf, young companions, young brown dwarfs (β and γ dwarfs) and members of the TWA. The young object 2M0355 (number 10) is marked with a green star. We overplot with coloured half circles joined by coloured dashed lines the EW predicted by the BT-Settl models 2014 for different gravities. We use the same colour code as for Fig. 8.

Na I (818.3 nm), Na I (819.5 nm), and Cs I (852.0 nm). In the NIR, we measured the K I (1253 nm) line.

In Fig. 8, we plot the equivalent width of the alkali lines in the optical for the objects in our sample, for objects from Chiu et al. (2006), Golimowski et al. (2004), Knapp et al. (2004), and Lodieu et al. (2015) versus their spectral types. We previously degraded the spectral resolution of the spectra and the models to the X-Shooter resolution. In Fig. 9, we plot equivalent widths of the K I line for our objects. We overplot field objects (McLean et al. 2003; Cushing et al. 2005), objects that belong to TW Hydrae Association (TWA), young companions (Allers & Liu 2007; Bonnefoy et al. 2014), young β-dwarfs and γ-dwarfs as a comparison (Allers & Liu 2007). We previously degraded the resolution of the observational spectra and the models to $R \sim 700$, which is the lowest resolution of all the spectra for which we calculate K I (1253 nm) equivalent width.

We overplot the equivalent width predicted by the BT-Settl models 2014 for those alkali lines. We transform previously the effective temperature of the models to spectral types, using the empirical relation between spectral types and effective temperature relation published in Stephens et al. (2009).

In the optical, the theory of cool atmospheres predicts the disappearance of the alkali elements in neutral form at temperatures below the L–T transition. This is a consequence of the depletion of the alkali atoms into molecular compounds, and the veiling by silicate clouds forming above the line-forming level, where the BT-Settl models 2014 overestimate the dust scattering. The apparent strength of the Na I subordinate lines decreases with spectra types from the early Ls through the T dwarfs. The equivalent width of Cs I (852.0 nm) increases from L0 to L9 and it is maximum for the early-T brown dwarfs, and it weakens progressively from the early-to-the-late T brown dwarfs. The BT-Settl models reproduce the evolution of the equivalent width with the spectral type for Rb I (794.8 nm) and Cs I (852.0 nm) lines, but underestimate the equivalent width of Na I (818.3 nm) and Na I (819.5 nm) lines, especially in early to mid-L dwarfs. These elements do not participate directly in the sedimentation and dust formation, therefore the offset between the predicted and the observed equivalent widths could be due to uncertainties in the cloud model or the dust opacity contributing to pseudo-continuum that defines the equivalent width.

Table 7. Equivalent widths in nm for alkali lines measured in the optical and in the NIR.

Name	Rb I (794.8 nm)	Na I (818.3 nm)	Na I (819.5 nm)	Cs I (852.0 nm)	K I (1253 nm)
LHS 102B	1.19 ± 0.01	0.31 ± 0.01	0.38 ± 0.01	0.69 ± 0.01	0.79 ± 0.01
2MASS J00361617+1821104	0.53 ± 0.01	0.21 ± 0.01	0.24 ± 0.01	0.34 ± 0.01	0.93 ± 0.01
2MASS J00531899−3631102	0.60 ± 0.09	0.16 ± 0.02	0.22 ± 0.02	0.35 ± 0.01	0.85 ± 0.01
SIMP 01365662+0933473	<0.3	0.06 ± 0.02	<0.06	0.65 ± 0.02	0.83 ± 0.01
2MASS J01443536−0716142				0.43 ± 0.09	0.82 ± 0.02
2MASS J02182913−3133230	<0.09	0.17 ± 0.02	0.19 ± 0.02	0.31 ± 0.01	0.79 ± 0.01
DENIS-P J0255.0−4700	<0.18	0.13 ± 0.01	0.19 ± 0.02	1.04 ± 0.02	0.45 ± 0.01
2MASS J02572581−3105523	<0.54		0.15 ± 0.05	0.53 ± 0.03	0.54 ± 0.01
2MASS J03480772−6022270	<0.46	<0.28	<0.013	0.47 ± 0.09	0.42 ± 0.01
2MASS J03552337+1133437	<0.03	0.08 ± 0.03	0.12 ± 0.01	0.29 ± 0.01	0.28 ± 0.01
SDSS J0423485−041403	0.77 ± 0.27	0.09 ± 0.02	0.07 ± 0.01	0.59 ± 0.02	0.67 ± 0.01
2MASS J04390101−2353083	<0.28	0.17 ± 0.03	0.21 ± 0.04	0.57 ± 0.02	0.72 ± 0.01
2MASS J04532647−1751543	<0.15	0.21 ± 0.05	0.19 ± 0.04	0.25 ± 0.03	0.70 ± 0.01
2MASS J05002100+0330501	0.64 ± 0.31	0.21 ± 0.01	0.24 ± 0.01	0.37 ± 0.01	0.81 ± 0.01
2MASS J05395200−0059019	0.83 ± 0.03	0.19 ± 0.01	0.20 ± 0.02	0.54 ± 0.01	0.89 ± 0.01
2MASS J06244595−4521548	<0.61	0.16 ± 0.02	0.19 ± 0.03	0.48 ± 0.02	0.70 ± 0.01
Gl 229B					0.24 ± 0.01
2MASS J10043929−3335189	0.75 ± 0.30	0.18 ± 0.02	0.22 ± 0.02	0.40 ± 0.02	0.85 ± 0.01
2MASS J11263991−5003550	0.75 ± 0.21	0.22 ± 0.01	0.24 ± 0.02	0.45 ± 0.02	1.05 ± 0.01
2MASS J13411160−3052505	0.37 ± 0.28	0.19 ± 0.02	0.25 ± 0.01	0.21 ± 0.01	0.64 ± 0.01
2MASS J18283572−4849046				0.60 ± 0.07	0.71 ± 0.01
2MASS J21513839−4853542				0.55 ± 0.16	0.98 ± 0.01

In the NIR (see Fig. 9), the equivalent width of the K I (1253 nm) has two peaks at around L4 and T4, with a minimum at about L8. This might reflect that as for the potassium, we see different atmospheric layers for the various subtypes (Faherty et al. 2014). Object 2M0355 (object 10) has weaker alkali lines in the optical and in the NIR, as it is a young object (Allers & Liu 2007; Faherty et al. 2012; Zapatero Osorio et al. 2014). The BT-Settl models reproduce the weakening of the K I (1253 nm) line for low-gravity objects, but overestimates the equivalent width of this line for field objects. In the L–T transition, the K I (1253 nm) depletion or molecular blanketing is overestimated.

In Table 7, we report the measured equivalent widths of the alkali lines for our sample. We do not report the equivalent widths for those alkali lines that were not detected in some of the targets.

7 CONCLUSIONS

We observed and analysed medium resolution VLT/X-Shooter spectra of 22 brown dwarfs with spectral types between L3 and T7. Objects in our sample have peculiar spectral characteristics or different classifications in the optical and in the NIR. Two of them are known binaries, that allow us to test our analysis.

Using Burgasser et al. (2006, 2010) and Bardalez Gagliuffi et al. (2014) empirical methods, we selected six objects as potential L plus T binary candidates: SIMP0136, SD0423, and DE0255, and 2M1341, 2M0053, and 2M0257. We compared these six objects with single field brown dwarfs (McLean et al. 2003; Cushing et al. 2005 and Spex libraries) and synthetic binaries. We found the best matches using a statistical analysis similar to the χ^2 analysis. Objects SIMP0136, 2M0257, and 2M1341 were discarded as candidates. The binarity hypothesis is weakened for object DE0255, due to their lack of overluminosity in the CMD, expected for late-L and early-T dwarf companions.

We tested the efficiency of the method described in Section 3, and the possible proportion of false positives introduced applying this method. To this aim, we compared single L and T dwarf spectra, and synthetic L plus T spectra, to other L and T single dwarf spectra, and to other synthetic L plus T binaries. We obtained that most of the L plus T synthetic binaries satisfy the binarity criteria. Nevertheless, 21 per cent of the L plus T synthetic binaries were not detected, i.e. 21 per cent of those synthetic binaries are missed when we apply the method described in Section 3 using a 99 per cent confidence level. 37 per cent of the single L dwarfs, and 35 per cent of the single T dwarfs satisfied the binarity criteria as well. The brown dwarf binary candidates found with this method should be confirmed using additional data.

We examined the possibility of finding equal spectral type brown dwarfs binaries. We compared single and synthetic binary spectra with the same subspectral type, to other single and synthetic binary spectra. For both cases, we obtained best matches with synthetic binary spectra for most of the cases. Therefore, we concluded that we are not able to find equal spectral type binary systems using this method. Additional data, such as parallax measurements, high-resolution imaging, or high-resolution spectra are necessary in order to find these systems.

We recalculated a lower limit for the very low mass binary fraction of $9.1^{+9.9}_{-3.0}$ per cent for our sample. We found that at least $4.5^{+10.4}_{-4.3}$ per cent of the L and T objects in our sample may be unresolved binaries with one L and one T possible members. This corresponds to a mass ratio of $q \geq 0.5$ for an age of a few Gyr (expected for most investigated objects). This percentage agrees with previous results.

BT-Settl models 2014 were able to reproduce the majority of the SEDs of our objects in the optical and in the NIR. None the less, these models usually failed to reproduce the shape of the *H* band, due to incomplete opacities for the FeH molecule in BT-Settl 2014 models. Best matches to models gave a range of effective temperatures between 950 K (T7) and 1900 K (L6.5), a range of gravities between 4.0 and 5.5. Some of the best matches corresponded to supersolar metallicity.

We measured the equivalent width of alkali lines with good signal-to-noise (Na I, K I, Rb I, and Cs I) in the optical and in the NIR spectra. We concluded that in the transition from L to T spectral types, the Na I doublet at 818.3 and 819.5 nm in the optical is

the first to disappear, while the other alkalines are present in the optical and NIR in the whole L–T spectral types. We overplotted the equivalent widths predicted by the BT-Settl models for those lines. The BT-Settl models reproduce the evolution of the equivalent width with the spectral type for the Rb I and Cs I lines, and the weakening of the K I line for the early L with low gravity. Nevertheless, the models underestimate the equivalent width of the Na I, lines in the optical, and overestimate the equivalent width for the K I line for field objects. These elements do not participate directly in the sedimentation and dust formation. Therefore, the differences between models and observational equivalent widths may be due to uncertainties in the cloud model or in the dust opacities.

The optical and NIR spectra reported in this paper will serve as templates for future studies in any of these wavelengths. In the near future, the *Gaia* satellite will release high-precision parallaxes of more than one billion of objects in the Milky Way, including hundreds of brown dwarfs. These parallaxes will allow us to detect the overluminosity of brown dwarf binaries with respect to single brown dwarfs.

ACKNOWLEDGEMENTS

Based on observations of ESO, using VLT/ESO, under the programmes 084.C-1092(A), 085.C-0862(A), and 085.C-0862(B). We gratefully acknowledge our referee, Daniella Bardalez-Gagliuffi, for her constructive inputs. We thank ESO allocation time committee and Paranal Observatory staff for performing these observations. We thank Adam Burgasser for providing and maintaining The SpeX Prism Spectral Libraries: http://pono.ucsd.edu/~adam/browndwarfs/spexprism/. We thank Adam Burgasser, Daniella Bardalez Gagliuffi, Jackie Radigan, Bram Venemans, and Esther Buenzli for their contribution in the development of this paper. This work was supported by Sonderforschungsbereich SFB 881 'The Milky Way System' (subprojects A4 and B6) of the German Research Foundation (DFG). This research has made use of the SIMBAD data base, operated at CDS, Strasbourg, France.

DH acknowledges support from the European Research Council under the European Community's Seventh Framework Programme (FP7/2007-2013 Grant Agreement no. 247060). The brown dwarf atmosphere models and synthetic spectra have been calculated at the Pôle Scientifique de Modélisation Numérique (PSMN) of the École Normale Supérieure de Lyon, and at the Gesellschaft für Wissenschaftliche Datenverarbeitung Göttingen (GWDG) in cooperation with the Institut für Astrophysik Göttingen. VJSB is supported by the project AYA2010-20535 from the Spanish Ministry of Economy and Competitiveness (MINECO).

REFERENCES

Abel M., Frommhold L., Li X., Hunt K. L. C., 2011, J. Phys. Chem. A, 115, 6805
Alcalá J. M. et al., 2014, A&A, 561, A2
Allard F., Hauschildt P. H., Alexander D. R., Tamanai A., Schweitzer A., 2001, ApJ, 556, 357
Allard F., Guillot T., Ludwig H.-G., Hauschildt P. H., Schweitzer A., Alexander D. R., Ferguson J. W., 2003a, in Martín E., ed., Proc. IAU Symp. 211, Brown Dwarfs. Astron. Soc. Pac., San Francisco, p. 325
Allard N. F., Allard F., Hauschildt P. H., Kielkopf J. F., Machin L., 2003b, A&A, 411, L473
Allard F., Allard N. F., Homeier D., Kielkopf J., McCaughrean M. J., Spiegelman F., 2007, A&A, 474, L21
Allard F., Homeier D., Freytag B., 2011, in Johns-Krull C., Browning M. K., West A. A., eds, ASP Conf. Ser. Vol. 448, 16th Cambridge Workshop on Cool Stars, Stellar Systems, and the Sun. Astron. Soc. Pac., San Francisco, p. 91
Allard F., Homeier D., Freytag B., Sharp C. M., 2012a, in Reylé C., Charbonnel C., Schultheis M., eds, EAS Publ. Ser. Vol. 57, Low-Mass Stars and the Transition Stars/Brown Dwarfs - Evry Schatzman School on Stellar Physics XXIII. EDP Sciences, Les Ulis, p. 3
Allard F., Homeier D., Freytag B., 2012b, Phil. Trans. R. Soc. A, 370, 2765
Allen P. R., 2007, ApJ, 668, 492
Allers K. N., Liu M. C., 2007, BAAS, 39, 103.15
Allers K. N., Liu M. C., 2013, ApJ, 772, 79
Andrei A. H. et al., 2011, AJ, 141, 54
Antonova A., Hallinan G., Doyle J. G., Yu S., Kuznetsov A., Metodieva Y., Golden A., Cruz K. L., 2013, A&A, 549, A131
Apai D., Radigan J., Buenzli E., Burrows A., Reid I. N., Jayawardhana R., 2013, ApJ, 768, 121
Artigau É., Doyon R., Lafrenière D., Nadeau D., Robert J., Albert L., 2006, ApJ, 651, L57
Artigau É., Bouchard S., Doyon R., Lafrenière D., 2009, ApJ, 701, 1534
Barber R. J., Tennyson J., Harris G. J., Tolchenov R. N., 2006, MNRAS, 368, 1087
Bardalez Gagliuffi D. C. et al., 2014, ApJ, 794, 143
Blake C. H., Charbonneau D., White R. J., 2010, ApJ, 723, 684
Bonnefoy M., Chauvin G., Rojo P., Allard F., Lagrange A.-M., Homeier D., Dumas C., Beuzit J.-L., 2010, A&A, 512, A52
Bonnefoy M. et al., 2013, A&A, 555, A107
Bonnefoy M., Chauvin G., Lagrange A.-M., Rojo P., Allard F., Pinte C., Dumas C., Homeier D., 2014, A&A, 562, A127
Bouy H., Brandner W., Martín E. L., Delfosse X., Allard F., Basri G., 2003, AJ, 126, 1526
Burgasser A. J., 2007, ApJ, 659, 655
Burgasser A. J. et al., 1999, ApJ, 522, L65
Burgasser A. J. et al., 2002, ApJ, 564, 421
Burgasser A. J., Kirkpatrick J. D., Reid I. N., Brown M. E., Miskey C. L., Gizis J. E., 2003, ApJ, 586, 512
Burgasser A. J., McElwain M. W., Kirkpatrick J. D., Cruz K. L., Tinney C. G., Reid I. N., 2004, AJ, 127, 2856
Burgasser A. J., Reid I. N., Leggett S. K., Kirkpatrick J. D., Liebert J., Burrows A., 2005, ApJ, 634, L177
Burgasser A. J., Geballe T. R., Leggett S. K., Kirkpatrick J. D., Golimowski D. A., 2006, ApJ, 637, 1067
Burgasser A. J., Cruz K. L., Kirkpatrick J. D., 2007, ApJ, 657, 494
Burgasser A. J., Looper D. L., Kirkpatrick J. D., Cruz K. L., Swift B. J., 2008, ApJ, 674, 451
Burgasser A. J., Cruz K. L., Cushing M., Gelino C. R., Looper D. L., Faherty J. K., Kirkpatrick J. D., Reid I. N., 2010, ApJ, 710, 1142
Burgasser A. J., Bardalez-Gagliuffi D. C., Gizis J. E., 2011, AJ, 141, 70
Burgasser A. J. et al., 2015, AJ, 149, 104
Burrows A., Sharp C. M., 1999, ApJ, 512, 843
Caffau E., Ludwig H.-G., Steffen M., Freytag B., Bonifacio P., 2011, Sol. Phys., 268, 255
Castro P. J., Gizis J. E., Harris H. C., Mace G. N., Kirkpatrick J. D., McLean I. S., Pattarakijwanich P., Skrutskie M. F., 2013, ApJ, 776, 126
Chiu K., Fan X., Leggett S. K., Golimowski D. A., Zheng W., Geballe T. R., Schneider D. P., Brinkmann J., 2006, AJ, 131, 2722
Close L. M., Siegler N., Freed M., Biller B., 2003, ApJ, 587, 407
Cohen M., Wheaton W. A., Megeath S. T., 2003, AJ, 126, 1090
Costa E., Méndez R. A., Jao W.-C., Henry T. J., Subasavage J. P., Ianna P. A., 2006, AJ, 132, 1234
Cruz K. L., Reid I. N., Liebert J., Kirkpatrick J. D., Lowrance P. J., 2003, AJ, 126, 2421
Cruz K. L., Kirkpatrick J. D., Burgasser A. J., 2009, AJ, 137, 3345
Cushing M. C., Rayner J. T., Vacca W. D., 2005, ApJ, 623, 1115
Cushing M. C. et al., 2008, ApJ, 678, 1372
Cutri R. M. et al., 2003, VizieR Online Data Catalog, 2246, 0
Dahn C. C. et al., 2002, AJ, 124, 1170
Dupuy T. J., Liu M. C., 2012, ApJS, 201, 19

Ellis S. C., Tinney C. G., Burgasser A. J., Kirkpatrick J. D., McElwain M. W., 2005, AJ, 130, 2347
Faherty J. K., Burgasser A. J., Cruz K. L., Shara M. M., Walter F. M., Gelino C. R., 2009, AJ, 137, 1
Faherty J. K. et al., 2012, ApJ, 752, 56
Faherty J. K., Rice E. L., Cruz K. L., Mamajek E. E., Núñez A., 2013, AJ, 145, 2
Faherty J. K., Beletsky Y., Burgasser A. J., Tinney C., Osip D. J., Filippazzo J. C., Simcoe R. A., 2014, ApJ, 790, 90
Folkes S. L., Pinfield D. J., Kendall T. R., Jones H. R. A., 2007, MNRAS, 378, 901
Freytag B., Allard F., Ludwig H.-G., Homeier D., Steffen M., 2010, A&A, 513, A19
Freytag B., Steffen M., Ludwig H.-G., Wedemeyer-Böhm S., Schaffenberger W., Steiner O., 2012, J. Comput. Phys., 231, 919
Gagné J., Lafrenière D., Doyon R., Malo L., Artigau É., 2014, ApJ, 783, 121
Gelino C. R., Marley M. S., Holtzman J. A., Ackerman A. S., Lodders K., 2002, ApJ, 577, 433
Gizis J. E., 2002, ApJ, 575, 484
Gizis J. E., Kirkpatrick J. D., Wilson J. C., 2001, AJ, 121, 2185
Gizis J. E., Reid I. N., Knapp G. R., Liebert J., Kirkpatrick J. D., Koerner D. W., Burgasser A. J., 2003, AJ, 125, 3302
Goldman B., Bouy H., Zapatero Osorio M. R., Stumpf M. B., Brandner W., Henning T., 2008, A&A, 490, 763
Golimowski D. A. et al., 2004, AJ, 127, 3516
Hargreaves R. J., Hinkle K. H., Bauschlicher C. W., Jr, Wende S., Seifahrt A., Bernath P. F., 2010, AJ, 140, 919
Helling C., Dehn M., Woitke P., Hauschildt P. H., 2008, ApJ, 675, L105
Homeier D., Hauschildt P., Allard F., 2003, in Hubeny I., Mihalas D., Werner K., eds, ASP Conf. Ser. Vol. 288, Stellar Atmosphere Modeling. Astron. Soc. Pac., San Francisco, p. 357
Janson M. et al., 2012, ApJ, 754, 44
Joergens V., 2008, A&A, 492, 545
Kendall T. R., Delfosse X., Martín E. L., Forveille T., 2004, A&A, 416, L17
Kirkpatrick J. D. et al., 2008, ApJ, 689, 1295
Kirkpatrick J. D. et al., 2011, ApJS, 197, 19
Knapp G. R. et al., 2004, AJ, 127, 3553
Koen C., Tanabé T., Tamura M., Kusakabe N., 2005, MNRAS, 362, 727
Leggett S. K., Toomey D. W., Geballe T. R., Brown R. H., 1999, ApJ, 517, L139
Leggett S. K. et al., 2000, ApJ, 536, L35
Liebert J., Kirkpatrick J. D., Cruz K. L., Reid I. N., Burgasser A., Tinney C. G., Gizis J. E., 2003, AJ, 125, 343
Lodders K., 1999, ApJ, 519, 793
Lodieu N., Zapatero Osorio M. R., Rebolo R., Bejar V. J. S., Pavlenko Y., Perez-Garrido A., 2015, A&A, 581, A73
Ludwig H.-G., Allard F., Hauschildt P. H., 2002, A&A, 395, 99
Ludwig H.-G., Allard F., Hauschildt P. H., 2006, A&A, 459, 599
Luhman K. L., Allers K. N., Jaffe D. T., Cushing M. C., Williams K. A., Slesnick C. L., Vacca W. D., 2007, ApJ, 659, 1629
Lunine J. I., Hubbard W. B., Marley M. S., 1986, ApJ, 310, 238
McLean I. S., McGovern M. R., Burgasser A. J., Kirkpatrick J. D., Prato L., Kim S. S., 2003, ApJ, 596, 561
Manjavacas E. et al., 2014, A&A, 564, A55
Marley M., 2000, in Griffith C. A., Marley M. S., eds, ASP Conf. Ser. Vol. 212, From Giant Planets to Cool Stars. Astron. Soc. Pac., San Francisco, p. 152
Marley M. S., Seager S., Saumon D., Lodders K., Ackerman A. S., Freedman R. S., Fan X., 2002, ApJ, 568, 335
Marocco F. et al., 2013, AJ, 146, 161
Martín E. L., Delfosse X., Basri G., Goldman B., Forveille T., Zapatero Osorio M. R., 1999, AJ, 118, 2466
Martín E. L. et al., 2010, A&A, 517, A53
Morales-Calderón M. et al., 2006, ApJ, 653, 1454
Nakajima T., Oppenheimer B. R., Kulkarni S. R., Golimowski D. A., Matthews K., Durrance S. T., 1995, Nature, 378, 463
Oppenheimer B. R., Golimowski D. A., Kulkarni S. R., Matthews K., Nakajima T., Creech-Eakman M., Durrance S. T., 2001, AJ, 121, 2189
Parker S. R., Tinney C. G., 2013, MNRAS, 430, 1208
Patience J., King R. R., De Rosa R. J., Vigan A., Witte S., Rice E., Helling C., Hauschildt P., 2012, A&A, 540, A85
Plez B., 2008, Phys. Scr. T, 133, 014003
Radigan J., Jayawardhana R., Lafrenière D., Artigau É., Marley M., Saumon D., 2012, ApJ, 750, 105
Radigan J., Jayawardhana R., Lafrenière D., Dupuy T. J., Liu M. C., Scholz A., 2013, ApJ, 778, 36
Reid I. N., Cruz K. L., Burgasser A. J., Liu M. C., 2008a, AJ, 135, 580
Reid I. N., Cruz K. L., Kirkpatrick J. D., Allen P. R., Mungall F., Liebert J., Lowrance P., Sweet A., 2008b, AJ, 136, 1290
Rossow W. B., 1978, Icarus, 36, 1
Ruiz M. T., Leggett S. K., Allard F., 1997, ApJ, 491, L107
Schneider A. C., Cushing M. C., Kirkpatrick J. D., Mace G. N., Gelino C. R., Faherty J. K., Fajardo-Acosta S., Sheppard S. S., 2014, AJ, 147, 34
Smart R. L. et al., 2013, MNRAS, 433, 2054
Stephens D. C. et al., 2009, ApJ, 702, 154
Tanaka H. K. M., 2005, J. Atmos. Sol.-Terr. Phys., 67, 1544
Theodossiou E., Danezis E., 1991, Ap&SS, 183, 91
Tsuji T., Ohnaka K., Aoki W., Nakajima T., 1996, A&A, 308, L29
Vernet J. et al., 2011, A&A, 536, A105
Vrba F. J. et al., 2004, AJ, 127, 2948
Wilson J. C., Miller N. A., Gizis J. E., Skrutskie M. F., Houck J. R., Kirkpatrick J. D., Burgasser A. J., Monet D. G., 2003, in Martín E., ed., Proc. IAU Symp. 211, Brown Dwarfs. Astron. Soc. Pac., San Francisco, p. 197
Witte S., Helling C., Barman T., Heidrich N., Hauschildt P. H., 2011, A&A, 529, A44
Zapatero Osorio M. R., Béjar V. J. S., Miles-Páez P. A., Peña Ramírez K., Rebolo R., Pallé E., 2014, A&A, 568, A6

APPENDIX A: OBSERVING LOG

Table A1. Observing log: DIT is the integration time in each position of the slit, and NINT is the number of exposures.

Name	Date	Arm	DIT (s)	NINT	Seeing (arcsec)	Airmass	Notes
LHS102B	2009 October 16	VIS/NIR	290/300	4/4	1.0	1.05	
Hip000349	2009 October 16	VIS/NIR	6/5	1/1	1.16	1.31	B9V telluric standard
2M J0036+1821	2009 November 7	VIS/NIR	290/300	4/4	1.1	1.4	
Hip112022	2009 November 7	VIS/NIR	6/5	1/1	1.4	1.5	B2IV telluric standard
2M J0053−3631	2009 October 16	VIS/NIR	290/300	4/4	1.44	1.05	
Hip000349	2009 October 16	VIS/NIR	6/5	1/1	1.15	1.01	B9V telluric standard
SIMP J0136+0933	2009 December 14	VIS/NIR	290/300	4/4	0.9	1.2	
Hip021576	2009 December 14	VIS/NIR	6/5	1/1	1.1	1.05	B3V telluric standard
2M J0144−0716	2009 December 14	VIS/NIR	290/300	4/4	1.05	1.15	
Hip021576	2009 December 14	VIS/NIR	6/5	1/1	1.05	1.15	B6V telluric standard
2M J0218−3133	2010 January 4	VIS/NIR	290/300	4/4	1.05	1.15	
Hip009534	2010 January 4	VIS/NIR	6/5	1/1	1.1	1.1	B6V telluric standard
DE J0255−4700	2009 October 17	VIS/NIR	290/300	4/4	2.2	1.14	
Hip009549	2009 October 17	VIS/NIR	6/5	1/1	2.2	1.2	B6V telluric standard
2M J0348−6022	2009 October 16	VIS/NIR	290/300	12/12	1.7	1.3	
Hip012389	2009 October 16	VIS/NIR	6/5	1/1	1.7	1.3	B8V telluric standard
2M J0355+1133	2009 December 21	VIS/NIR	290/300	4/4	0.92	1.2	
Hip023060	2009 December 21	VIS/NIR	6/5	1/1	0.92	1.2	B2V telluric standard
SD J0423−0414	2009 December 26	VIS/NIR	290/300	4/4	0.8	1.4	
Hip020424	2009 December 26	VIS/NIR	6/5	1/1	0.9	1.4	B9V telluric standard
2M J0439−2353	2009 December 21	VIS/NIR	290/300	5/5	1.4	1.0	
Hip018926	2009 December 21	VIS/NIR	6/5	1/1	1.4	1.0	B3V telluric standard
2M J0453−1751	2009 December 21	VIS/NIR	290/300	8/8	1.1	1.1	
Hip023060	2009 December 21	VIS/NIR	6/5	1/1	1.1	1.1	B2V telluric standard
2M J0500+0330	2010 February 05	VIS/NIR	290/300	4/4	0.7	1.1	
Hip037623	2010 February 05	VIS/NIR	6/5	1/1	0.7	1.1	B5V telluric standard
SD J0539−0059	2010 January 17	VIS/NIR	290/300	4/4	0.7	1.1	
Hip033007	2010 January 17	VIS/NIR	6/5	1/1	0.7	1.1	B4V telluric standard
Gl229B	2009 December 14	VIS/NIR	290/300	4/4	1.2	1.4	
Hip044786	2009 December 14	VIS/NIR	6/5	1/1	1.2	1.4	B6V telluric standard
2M J0624−4521	2009 December 16	VIS/NIR	290/300	5/5	0.8	1.4	
Hip030175	2009 December 16	VIS/NIR	6/5	5/5	0.8	1.4	B9.5V telluric standard
2M J1004−3335	2010 February 5	VIS/NIR	290/300	4/4	0.9	1.0	
Hip057861	2010 February 5	VIS/NIR	6/5	1/1	0.9	1.0	B5V telluric standard
2M J1126−5003	2010 February 4	VIS/NIR	290/300	4/4	1.6	1.1	
Hip073345	2010 February 4	VIS/NIR	6/5	4/4	1.6	1.1	B5V telluric standard
2M J2151−4853	2010 May 08	VIS/NIR	290/300	10/10	1.4	1.2	
Hip111085	2010 May 08	VIS/NIR	6/5	10/10	1.4	1.2	B9V telluric standard
2M J1341−3052	2010 June 02	VIS/NIR	290/300	10/10	0.7	1.0	
Hip068124	2010 June 02	VIS/NIR	6/5	10/10	0.7	1.0	B9V telluric standard
2M J1828−4849	2010 June 06	VIS/NIR	290/300	10/10	1.5	1.4	
Hip092687	2010 June 06	VIS/NIR	6/5	1/1	1.5	1.4	B4III telluric standard

APPENDIX B: REDUCED SPECTRA

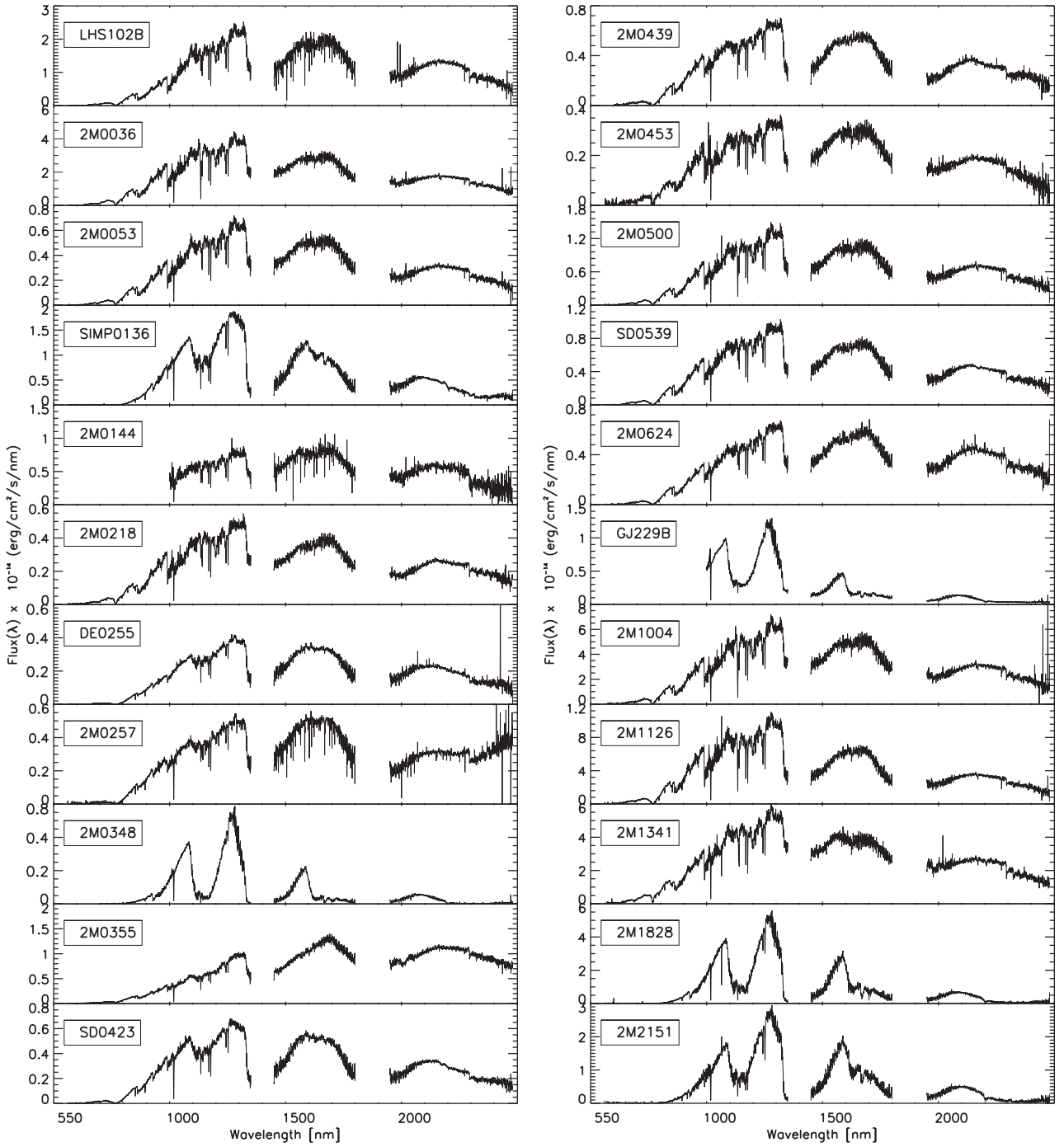

Figure B1. Spectra of our 22 targets after reduction and degrading them at $R \sim 1000$. Wavelengths largely affected by telluric absorption are removed from the figure in the NIR, as well as the optical part for object Gl229B, because it is contaminated by the flux of its companion and the optical part of 2M0144 because it is noisy. We plot spectra between 550 and 1350, 1450 and 1800, and 1950 and 2500 nm to avoid telluric absorptions.

APPENDIX C: SPECTRAL INDICES CRITERIA

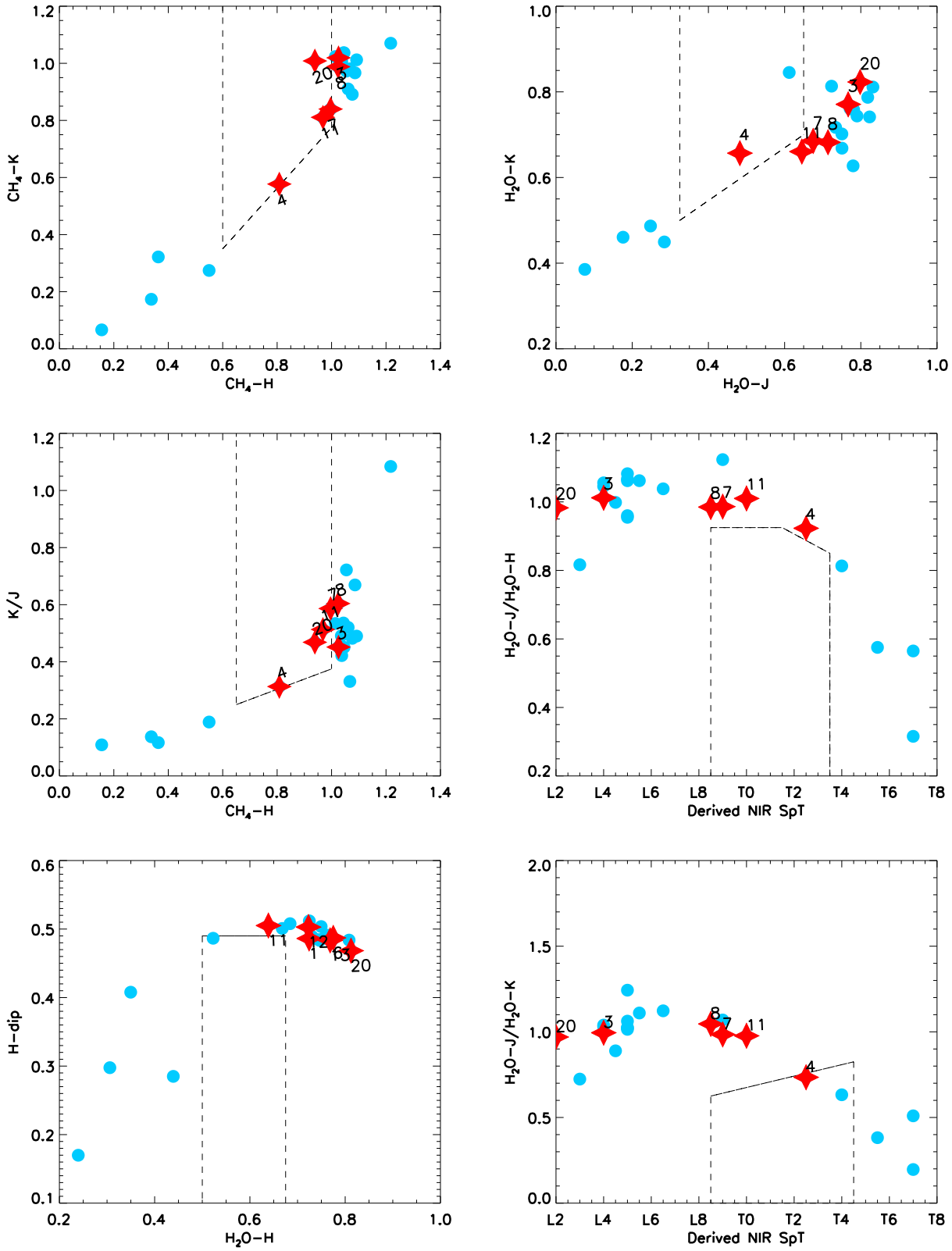

Figure C1. Spectral index selection. Numbers 1–22 correspond to our objects. The boxes shown with dashed lines mark the areas where the selection criteria of Table C1 are valid. The red stars represent objects satisfying more than four such criteria.

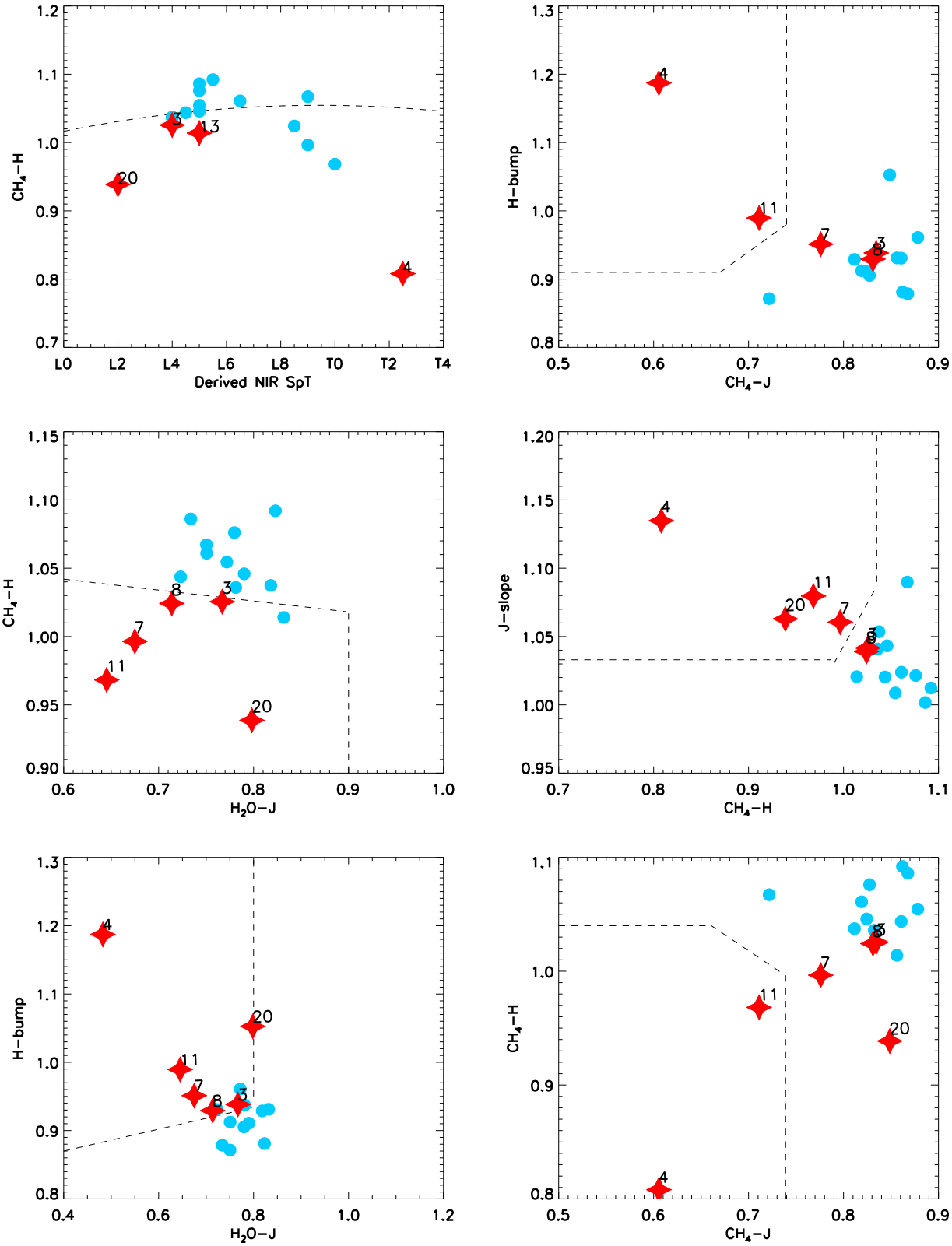

Figure C2. Spectral index selection.

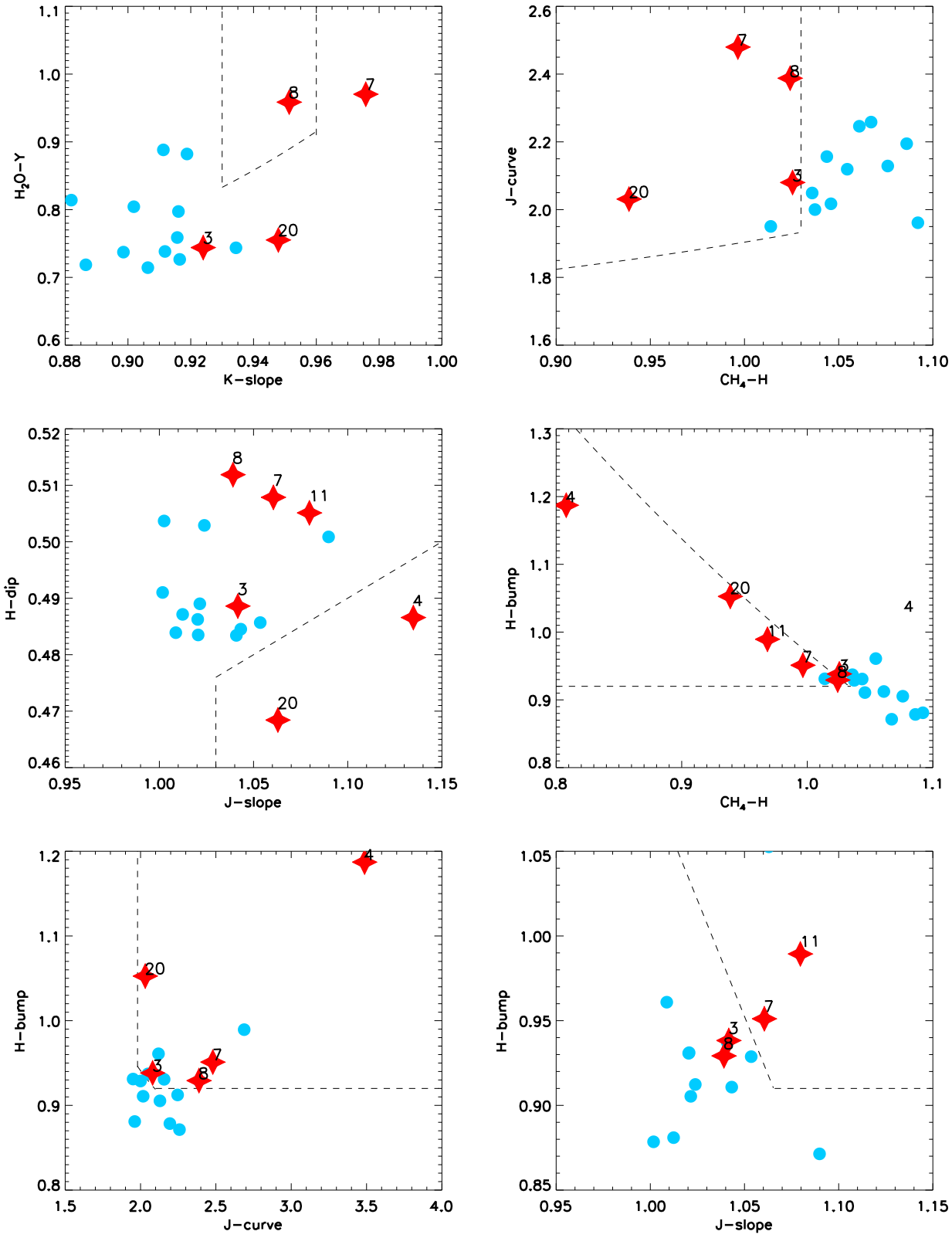

Figure C3. Spectral index selection.

Table C1. Spectral indices to select L plus T brown dwarf binary candidates.

Index	Numerator range[a]	Denominator range[a]	Feature	Reference
H_2O–*J*	1140–1165	1260–1285	1150 nm H_2O	1
CH_4–*J*	1315–1340	1260–1285	1320 nm CH_4	1
H_2O–*H*	1480–1520	1560–1600	1400 nm H_2O	1
CH_4–*H*	1635–1675	1560–1600	1650 nm CH_4	1
H_2O–*K*	1975–1995	2080–2100	1900 nm H_2O	1
CH_4–*K*	2215–2255	2080–2120	2200 nm CH_4	1
K/*J*	2060–2100	1250–1290	$J - K$ colour	1
H-dip	1610–1640	1560–1590 + 1660–1690[b]	1650 nm CH_4	2
K-slope	2.06–2.10	2.10–2.14	*K*-band shape/CIA H_2	3
J-slope	1.27–1.30	1.30–1.33	1.28-μm flux peak shape	4
J-curve	1.04–1.07+1.26–1.29[c]	1.14–1.17	Curvature across *J* band	4
H-bump	1.54–1.57	1.66–1.69	Slope across *H*-band peak	4
H_2O–*Y*	1.04–1.07	1.14–1.17	1.15 μm H_2O	4
Derived NIR SpT			Near-infrared spectral type[d]	1

Notes. [a]Wavelength range in nm over which flux density is integrated; [b]denominator is the sum of the flux in the two wavelength ranges; [c]numerator is the sum of the two ranges; [d]NIR spectral type derived using comparison to SpeX spectra.
References: 1 – Burgasser et al. (2006); 2 – Burgasser et al. (2010); 3 – Burgasser et al. (2002); 4 – Bardalez Gagliuffi et al. (2014).

Table C2. Index criteria for the selection of potential brown dwarf binary systems.

Abscissa	Ordinate	Inflection points
H_2O–*J*	H_2O–*K*	(0.325,0.5),(0.65,0.7)
CH_4–*H*	CH_4–*K*	(0.6,0.35),(1,0.775)
CH_4–*H*	*K*/*J*	(0.65,0.25),(1,0.375)
H_2O–*H*	*H*-dip	(0.5,0.49),(0.875,0.49)
Spex SpT	H_2O–*J*/H_2O–*H*	(L8.5,0.925),(T1.5,0.925),(T3,0.85)
Spex SpT	H_2O–*J*/CH_4–*K*	(L8.5,0.625),(T4.5,0.825)

Table C3. Delimiters for selection regions of potential brown dwarf binary systems.

Abscissa	Ordinate	Limits
SpT	CH_4–*H*	Best-fitting curve: $y = -4.3x10^{-4}x^2+0.0253x + 0.7178$
H_2O–*J*	CH_4–*H*	Intersection of: $-0.08x+1.09$ and $x = 0.90$
H_2O–*J*	*H*-bump	Intersection of: $y = 0.16x+0.806$ and $x = 0.90$
CH_4–*J*	CH_4–*H*	Intersection of: $y = -0.56x + 1.41$ and $y = 1.04$
CH_4–*J*	*H*-bump	Intersection of: $y = 1.00x + 0.24$, $x = 0.74$ and $y = 0.91$
CH_4–*H*	*J*-slope	Intersection of: $y = 1.250x - 0.207$, $x = 1.03$ and $y = 1.03$
CH_4–*H*	*J*-curve	Best-fitting curve: $y = 1.245x^2 - 1.565x + 2.224$
CH_4–*H*	*H*-bump	Best-fitting curve: $y = 1.36x^2 - 4.26x + 3.89$
J–slope	*H*-dip	Intersection of $y = 0.20x + 0.27$ and $x = 1.03$
J–slope	*H*-bump	Intersection of: $y = -2.75x + 3.84$ and $y = 0.91$
K–slope	H_2O–*Y*	Best-fitting curve: $y = 12.036x^2 - 20.000x + 8.973$
J–curve	*H*-bump	Best-fitting curve: $y = 0.269x^2 - 1.326 + 2.479$

APPENDIX D: BEST MATCHES TO POTENTIAL L PLUS T BINARIES

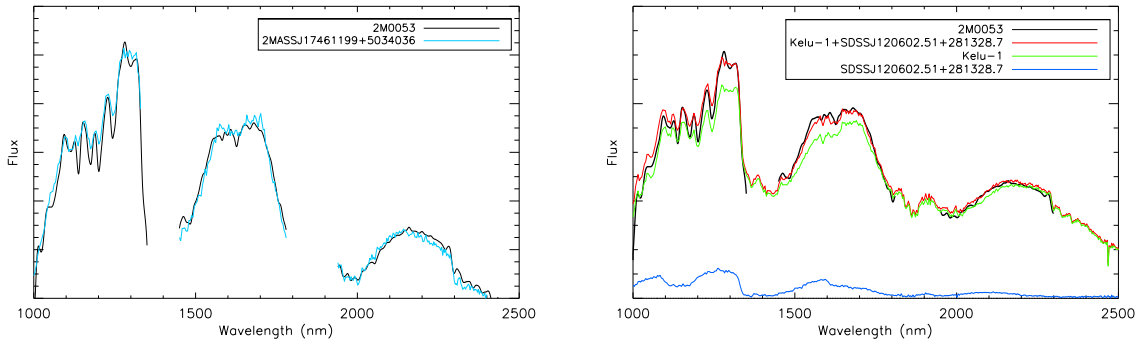

Figure D1. Best matches for object 2M0053 to single (left plot) and composite spectra (right plot). We show in black our X-Shooter spectra. In the plot on the left, the blue spectrum belongs to the best single match (2MASS 17461199+5034036; Reid et al. 2008a). In the plot on the right, we show in red the composite spectrum, in green the spectrum of the primary (Kelu-1; Ruiz, Leggett & Allard 1997) and in blue the spectra of the secondary (SDSS 120602.51+281328.7; from Chiu et al. 2006). $\eta_{SB} = 1.35$. The flux is $F(\lambda)$.

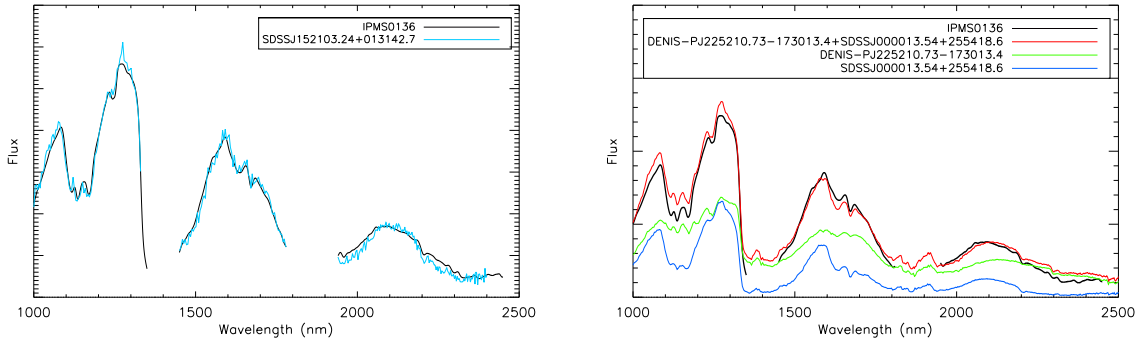

Figure D2. Best matches for object SIMP0136 (T2.5) to single (SDSS J152103.24+013142.7, from Knapp et al. 2004) and composite spectra (DENIS-PJ225210.73−173013, from Kendall et al. 2004; and SDSS J000013.54+255418.6, from Knapp et al. 2004). In black our smooth X-Shooter spectrum. Colours are the same as in Fig. D1. $\eta_{SB} = 0.55$. The flux is $F(\lambda)$.

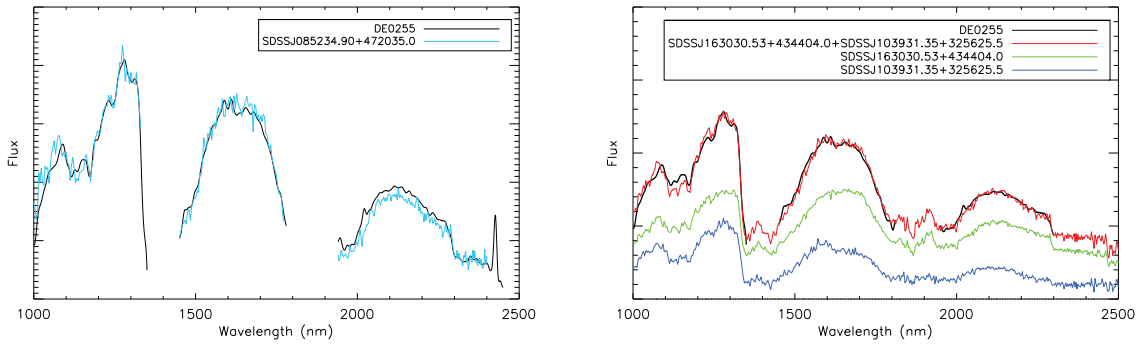

Figure D3. Best matches for object DE0255 (L9) using single (SDSS J085234.90+472035.0, from Knapp et al. 2004) and composite spectra (SDSS J163030.53+434404.0, from Knapp et al. 2004; and SDSS J103931.35+325625.5, from Chiu et al. 2006). Colours are the same as in Fig. D1. $\eta_{SB} = 3.42$. The flux is $F(\lambda)$.

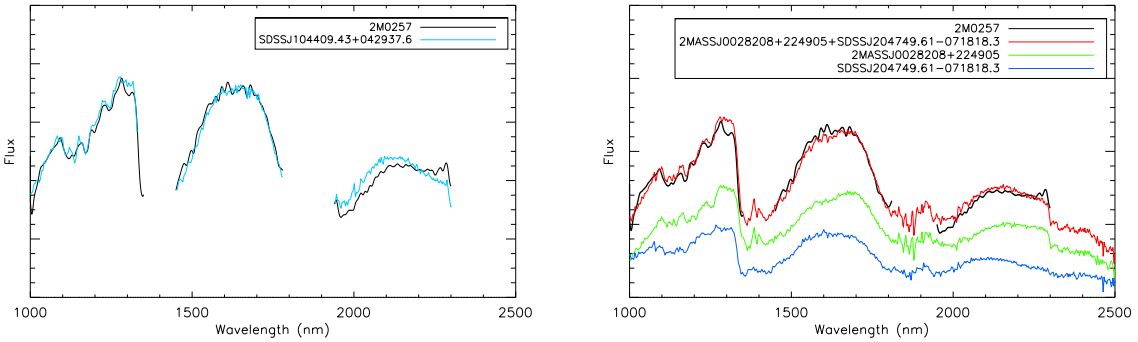

Figure D4. Best matches for object 2M0257 to single (SDSS J104409.43+042937.6, from Knapp et al. 2004) and composite spectra (2MASS J0028208+224905, from Cutri et al. 2003; and SDSS J204749.61−071818.3, from Knapp et al. 2004). Colours are the same as in Fig. D1. $\eta_{SB} = 1.23$. The flux is $F(\lambda)$.

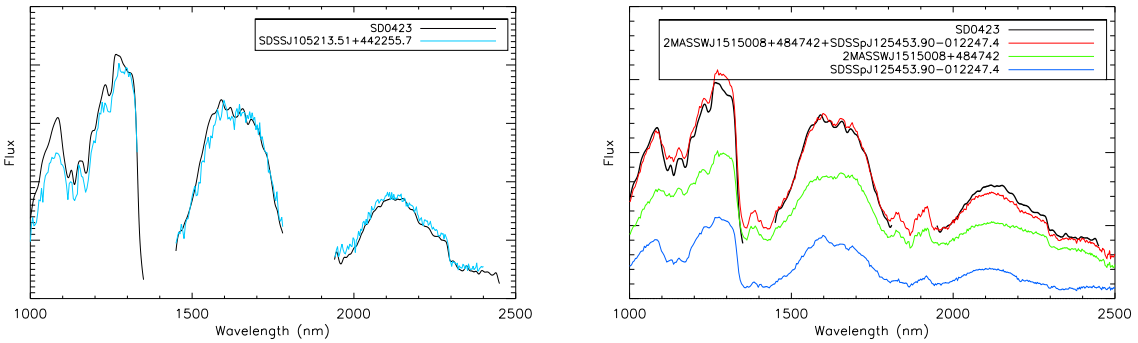

Figure D5. Best match for object SD0423 (T0) using single (SDSS J105213.51+442255.7, from Chiu et al. 2006) and composite spectra (2MASS J1515008+484742, from Wilson et al. 2003; and SDSS J125453.90−012247.4, from Leggett et al. 2000). Colours are the same as in Fig. D1. $\eta_{SB} = 3.423.23$. The flux is $F(\lambda)$.

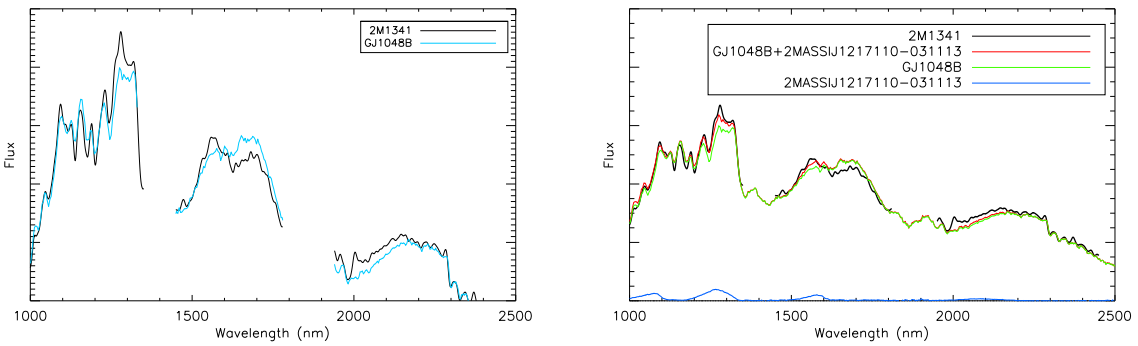

Figure D6. Best matches for object 2M1341 (L2, peculiar) to single (GJ1048B, from Gizis, Kirkpatrick & Wilson 2001) and composite spectra (GJ1048B, from Gizis et al. 2001; and 2MASS J1217110−031113, from Burgasser et al. 1999). Colours are the same as in Fig. D1. $\eta_{SB} = 1.26$. The flux is $F(\lambda)$.

APPENDIX E: BEST MATCHES TO BT-SETTL MODELS 2014

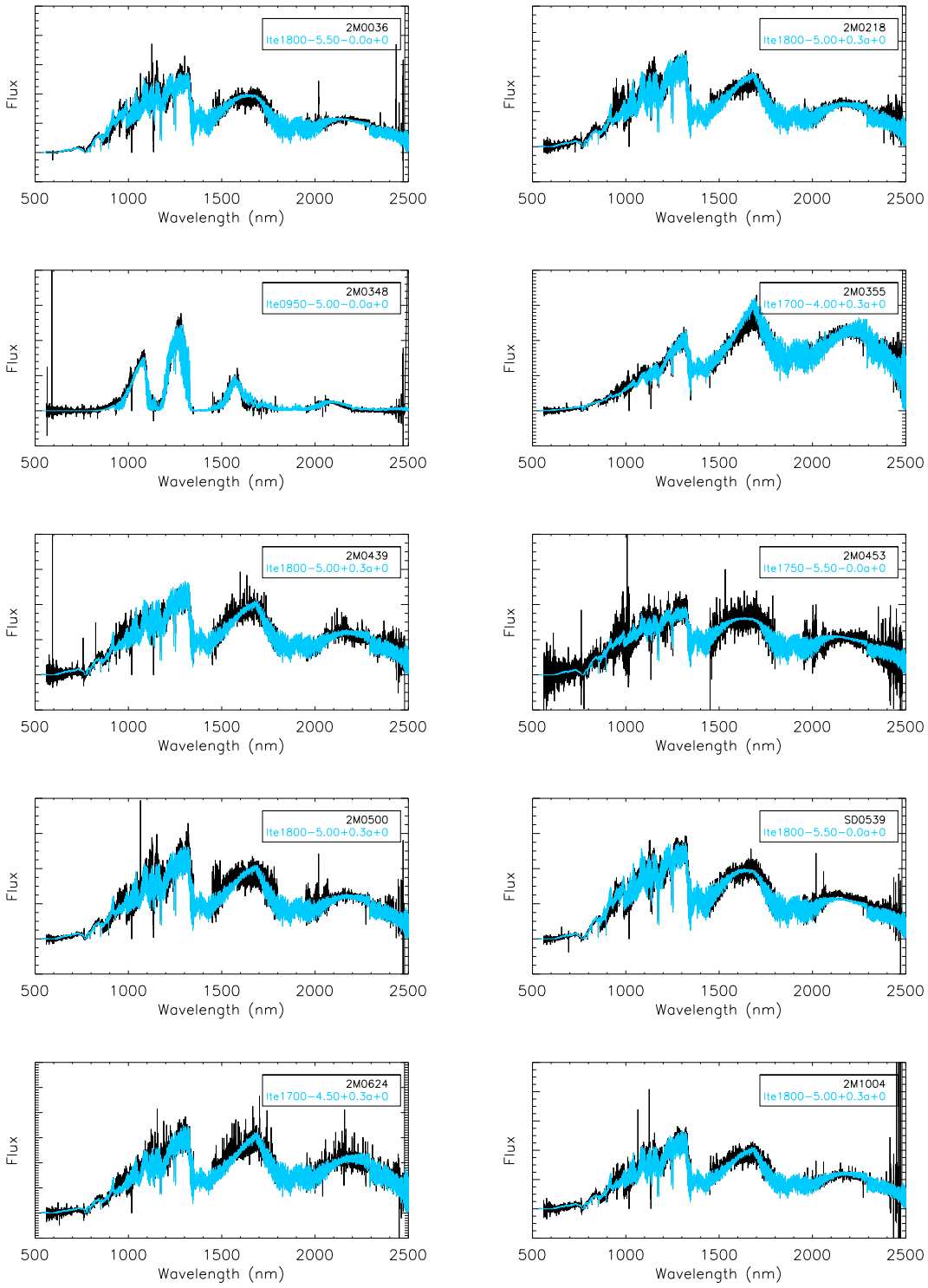

Figure E1. Best matches to BT-Settl models 2014 found using equation (1), as in Section 3.1. Effective temperature, gravity, metallicity, and alpha element enhancement are described in the model name strings as `lte-LOGG+[M/H]a+[ALPHA/H]`. The flux is $F(\lambda)$.

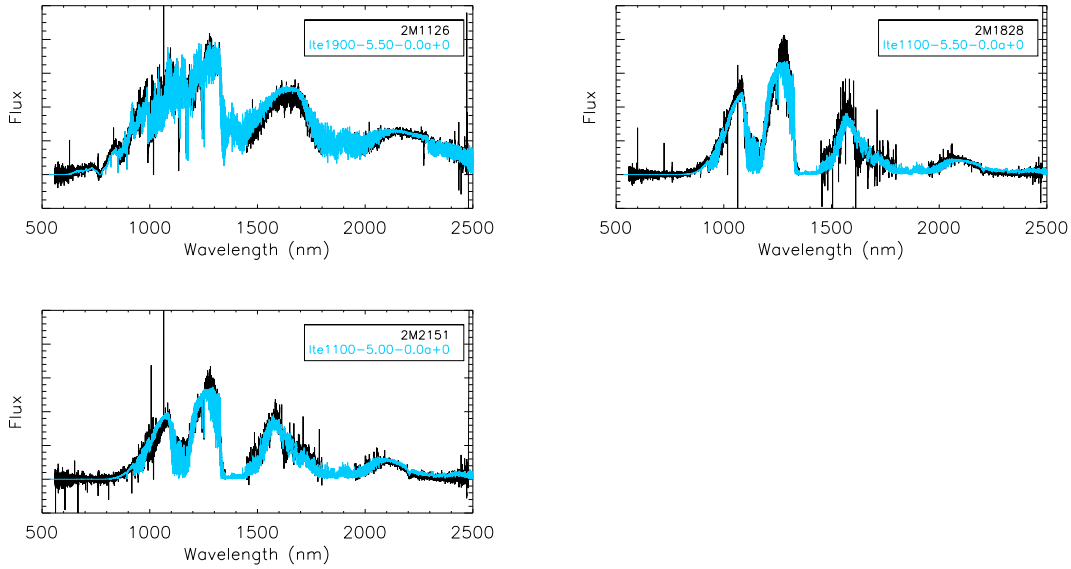

Figure E2. Best matches to BT-Settl models 2014 found using equation (1), as in Section 3.1. Effective temperature, gravity, metallicity, and alpha element enhancement are described in the model name strings as `lte-LOGG+[M/H]a+[ALPHA/H]`. The flux is $F(\lambda)$.

This paper has been typeset from a TEX/LATEX file prepared by the author.